ABSTRACT

Evaluating Approaches to Detecting Ice Accretion in and around Turbofan Jet Engines

George Diamond Toby, M.S.E.C.E.

Mentor: B. Randall Jean, Ph.D.

The accumulation of ice crystals in the compressor stages of a jet engine causes power loss events during flight that could potentially become catastrophic. The electromagnetic properties of ice clouds make them nearly undetectable to radars and hence the need for a new sensing technique. A microwave radiometer and two different types of interferometer sensors are being developed to address this issue. A microwave radiometer measures power that can be expressed as brightness temperature. Due to material properties, ice emits a significantly higher amount of energy and appears "brighter" to a microwave radiometer compared to liquid water. Interferometers, on the other hand, make highly sensitive measurements by superimposing electromagnetic waves and causing an interference. Results from various experiments conducted with the radiometer validated the design approach and served as proof of concept.

Evaluating Approaches to Detecting Ice Accretion in and around Turbofan Jet Engines

by

George Diamond Toby, B.S.E.E.

A Thesis

Approved by the Department of Electrical and Computer Engineering

_____

Kwang Y. Lee, Ph.D., Chairperson

Submitted to the Graduate Faculty of
Baylor University in Partial Fulfillment of the
Requirements for the Degree
of

Master of Science in Electrical and Computer Engineering

Approved by the Thesis Committee

_____

B. Randall Jean, Ph.D., Chairperson

_____

Jonathan Hu, Ph.D.

_____

Elyssia Gallagher, Ph.D.

_____

Brandon Herrera, Ph.D

Accepted by the Graduate School

August 2018

_____

J. Larry Lyon, Ph.D., Dean

Page bearing signatures is kept on file in the Graduate School.

TABLE OF CONTENTS

LIST OF FIGURES

LIST OF TABLES

ACKNOWLEDGMENTS

I would like to thank Dr. B. Randall Jean for his support, guidance and direction. Thank you also to Dr. Brandon Herrera, Tanner Trapp, Chris Faulkner, Sarvin Rezayat, Adam Lewis, and Justin Bui for their assistance. Moreover, thanks to DLT-2, LLC for their financial sponsorship of this work.

I would also like to thank the Toby, Hena, Green, Kliewer, Fiamahn, and Sirleaf families for their support and encouragement on this journey.

To my parents, Mrs. Angelyn Hena Toby, Dr. Christiana Koisey Hena, and Mr. Victor Toby

CHAPTER ONE
Introduction

Motivation

The accretion of ice particles in turbofan jet engines presents a safety problem that has remained unsolved for decades. Ice crystals accrete on stator vanes that redirect the air flow of the engine and on ducts with high turning angles [1]. When sufficient ice accretes, the engine experiences a "rollback," which refers to the uncommanded loss in engine thrust [2]. This loss in engine thrust is sometimes initially manifested by a gradual decay in engine fan rotational speed and a final stabilization of the engine at sub-idle operating conditions. Of over 240 icing related problems reported from 1990 to 2006, about 62 of the events were categorized as turbofan power-loss due to ice particle icing [1]. Fig. 1 shows a schematic of a turbofan jet engine and indicates the locations where ice particles accrete.

Ice crystals, which form ice clouds, can cause power loss and fan blade damage to aircraft engines when ingested. These particles span a range from less than 10 microns to a few centimeters and are mainly found at altitudes above 22,000 ft [1]. Ice crystals are formed when convective clouds transport low-level air high into the atmosphere where water-vapor condenses as the temperature drops. As the vapor rises higher, the temperature forces a change in state and ice particles are formed.

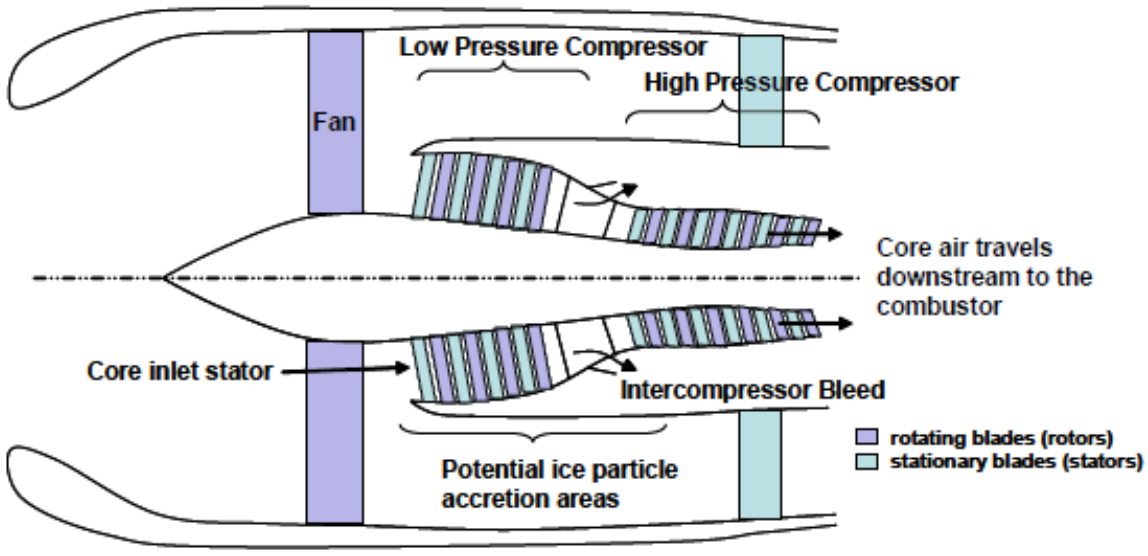

Fig. 1 - Turbofan Jet Engine Schematic [1]

To date, current methods and procedures for addressing ice accretion are inadequate. The onboard weather radar system on aircrafts remain incapable of detecting ice clouds because of their low radar reflectivity [1]. The current procedure for combatting ice accretion involves descending to a warmer temperature region and/or redirecting hot air from downstream to the low pressure compressor [1]. These maneuvers which are only performed when suspected by pilots are not only costly, but over time could cause damage to the low compressor stage of the aircraft.

A microwave sensing system is being researched by the Microwave Applied Metrology Lab at Baylor University to detect ice accretion in and around turbofan jet engines. The goal of the project is for the system to identify ice cloud environments and to ascertain whether or not ice is forming inside the engine. Sensors that can reliably detect ice cloud environments and internal icing are needed for improved flight safety [2].

CHAPTER TWO

Microwave Radiometry

Radiometry is concerned with the study of measurement methods of electromagnetic radiation [3, p. 1]. A microwave radiometer passively measures power which is often expressed in terms of a proportionate temperature. Microwave sensing is used in many different applications over a frequency range from about 300 MHz ($\lambda \approx 100\ cm$) to 300 GHz ($\lambda \approx 0.1\ cm$).

All objects are transmitters of electromagnetic radiation. The level of emission is dependent on the temperature of the object. The temperature detected by microwave radiometers, known as brightness temperature, is the temperature of a blackbody that would radiate an equivalent amount of power [4, p.3]. At any given temperature, black bodies radiate the largest amount of energy and absorb all thermal radiations incident upon them. Black body radiation at a particular temperature can be described by the Stefan – Boltzmann law. This law states that at a given temperature (T), per unit time and unit area, the sum total of all the energy emitted from the surface of a black body in all directions into the half space above the surface is proportional to the fourth power of the temperature [5, p.5]. This law is expressed mathematically as

$$M_e^b(T) = \sigma T^4, \tag{1}$$

where M_e^b is the total radiant exitance measured in watts per square meter and σ is the Stefan-Boltzmann constant. Although the above formula gives the total amount of energy emitted at any given temperature, it provides no information on wavelength dependency.

Kirchoff's function in (2) relates this radiation based on both wavelength and temperature [5, p.6].

$$M_{e,\lambda}^{b}(\lambda, T) = \frac{1}{\lambda^5} F(\lambda T), \tag{2}$$

where $F(\lambda T)$ is Kirchhoff's universal function.

The study of blackbodies and their radiation is significant in the understanding of radiometer systems and how measurements and classification of objects are made possible. At a certain bandwidth (B) and temperature (T), the power (P) of a blackbody emission is given by

$$P = k_B T B, \tag{3}$$

where k_B is the Boltzmann constant. The intensity of the radiation is given by Planck's law. The law describes the ideal spectral distribution of radiant energy based on the relationship to temperature and wavelength [6, p.6]. Mathematically, Planck's law is given by

$$B_f(T) = \frac{2hf^3}{c^2 e^{\frac{hf}{k_B T}} - 1}, \tag{4}$$

where $B_f(T)$ is the radiance, a function of both temperature and frequency, and given in units of $\frac{W}{m^2} \cdot sr \cdot Hz$. In (4), h is Planck's constant, f is the frequency in Hertz, c is the speed of light in vacuum and, T is the physical temperature in Kelvin [2, pg. 5].

Spectral radiance, also known as the brightness, is the quantity of energy radiated by a surface per unit area, per unit wavelength and at a specific angle. Radiation intensity in terms of both frequency and wavelength is given below in Fig. 2:

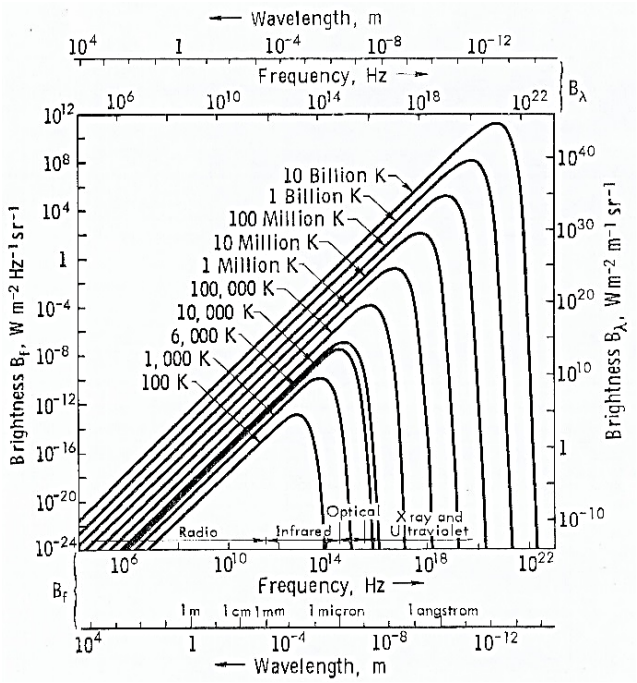

Fig. 2 - Planck's Law radiation curve as a function of frequency and wavelength [8, p.456]

The spectral radiance of an object corresponds to an associated physical temperature. The ability of real objects to radiate energy is characterized by emissivity. Emissivity is defined as the ratio of the total radiance of a real body to that of a blackbody. Spectral emissivity, ε, accounts for the wavelength dependence of emissivity and is expressed mathematically as

$$\varepsilon(\lambda) = \frac{L(\lambda,T)}{L_b(\lambda,T)}, \tag{5}$$

In (5), $L(\lambda,T)$ is the spectral radiance of the real object and $L_b(\lambda,T)$ is that of the blackbody. Spectral emissivity lies between 0 and 1 at any given wavelength λ. A value of 0 signifies zero radiation and a value of 1 corresponds to a radiation level equivalent to that of a blackbody [7, p.15].

Microwave radiometers incorporate a receiving antenna that aids the system in the detection of the varying emissivity of objects. The antenna collects energy that can be

expressed as an equivalent brightness temperature, T_A of the object being observed. The system processes a portion of the output power of the antenna within a bandwidth B around a given center frequency. The power is then boosted by a gain G and measured by the radiometer's detector circuits. The total power measured by the radiometer includes the desired value

$$P = k_B BGT_A. \quad (6)$$

However, the power in (6) does not take into account the thermal noise of objects in and around the radiometer. The power measured has to take into account the noise temperature (T_N) of the system. The actual power then becomes

$$P = k_B BG(T_A + T_N). \quad (7)$$

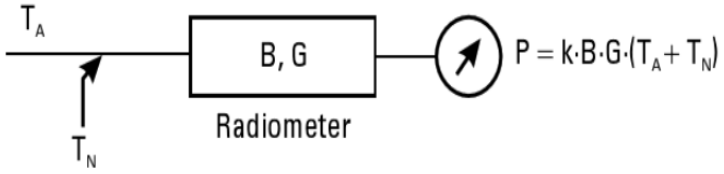

Fig. 3 - Model of a radiometer [4, p. 8]

Fig. 3 above shows the model of a radiometer that takes the noise temperature of the system into account. The power measured by the system is typically very low and on the order of picowatts; therefore, the noise presents a measuring problem that is addressed based on sensitivity. The sensitivity of a radiometer (ΔT) is improved by averaging the random noise signal over the integration time, τ.

$$\Delta T = \frac{T_A + T_N}{\sqrt{B \cdot \tau}} \quad (8)$$

Larger bandwidths and longer integration times are proportional to higher sensitivities. This is true since a smaller ΔT corresponds to a smaller brightness temperature change that can be detected by the radiometer.

Dicke Radiometer

A microwave radiometer has to be sensitive and possess gain and noise stability. One method for improving the stability of radiometers is the Dicke method. R.H. Dicke, in 1946, described a technique of detecting weak thermal radiation and noise-like signals limited by the receiver of the system [9, pg.1]. The Dicke radiometer is unique in that it does not directly measure the temperature of the antenna, but compares it to a known reference, T_R in the system. The input signal is rapidly switched between the output of the antenna and the known reference that is maintained at a relatively fixed temperature. The switching frequency, F_s, is usually about 1 KHz. The system also passes the signal through a square law detector before it is integrated. The square law detector outputs a signal that is proportional to the square of the input signal. Fig. 4 shows the model of the Dicke radiometer:

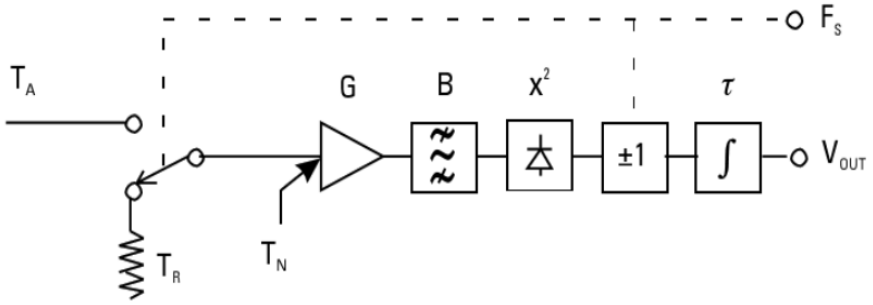

Fig. 4 - Model of a Dicke radiometer [4, p.14]

If the switching frequency of the system is fast enough, the temperature of the antenna, noise, and gain can be considered as constants over the measurement interval. Nevertheless, this improvement results in only half of the time being spent collecting the energy from the output of antenna thereby using only half of the integration time. The associated price of the enhanced stability is reduced sensitivity [4, p.14 - 15]. The sensitivity of the system becomes

$$\Delta T = \frac{T_A + T_N}{\sqrt{B \cdot \left(\frac{\tau}{2}\right)}} \tag{9}$$

An actual radiometer system is more detailed than the model in Fig. 4. The Dicke radiometer model in Fig. 5 includes front-end circuitry that selects a specific frequency band and amplifies the incoming signal before sending it to the low frequency circuitry. A super-heterodyne receiver allows for an increase in frequency selectivity. However, the system does not carry out all the amplification and selectivity at the input frequency. Instead, it partly selects a frequency band, usually very large, at the input to repress strong signals that are out of band. By doing this, it is ensured that other strong signals in the spectrum do not saturate the signal of the local oscillator because of the allowable voltage amplification range.

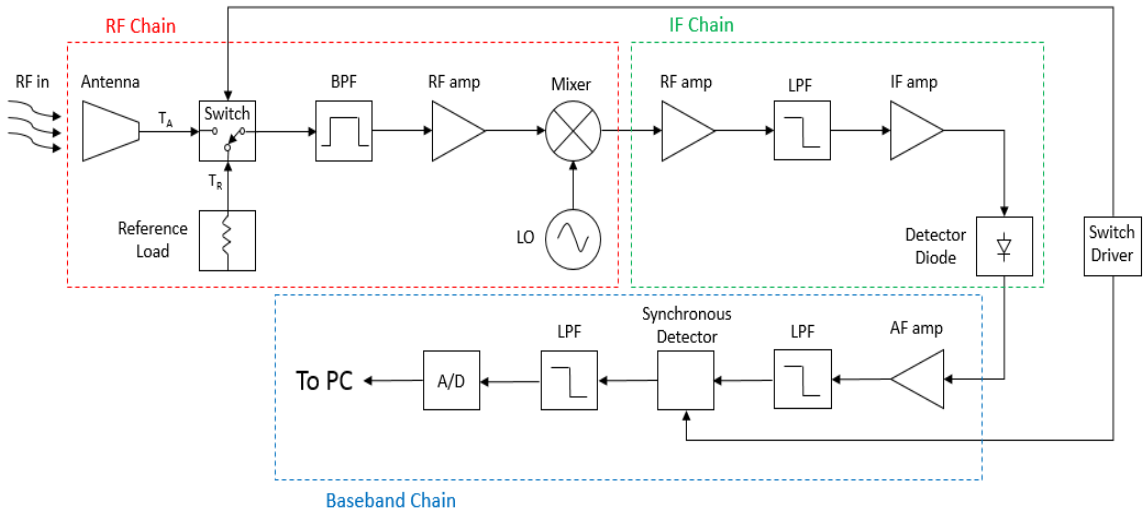

Fig. 5 - Detailed block diagram of a Dicke radiometer [9, p.8]

For any radiometer, the main selectivity happens in the IF chain and is achieved by the IF filter where the intermediate frequency is amplified before detection [4, p. 26 – 27]. The IF filter establishes the bandwidth of the radiometer. It usually does not start from DC since a 10 MHz high-pass filter is usually added into the filter sections. Schottky barrier diodes are commonly used as detectors since they yield a sensitivity of about 7 mV/µW. The sensitivity of the receiver refers to the weakest signal level that it can acquire and still be able to provide a satisfactory output quality. The sensitivity of receivers is usually expressed in dBm [10, p. 93].

The detector in the system changes the nature of the signal. Before detection, the signal is high frequency and has two levels that correspond to the position (Antenna or Reference) of the Dicke switch. After detection, only the amplitude levels of the signal,$T_R + T_N$ *or* $T_A + T_N$, is revealed. Moreover, the detector is AC-coupled and now consists of the information about the difference between T_R and T_A [4, p. 31].

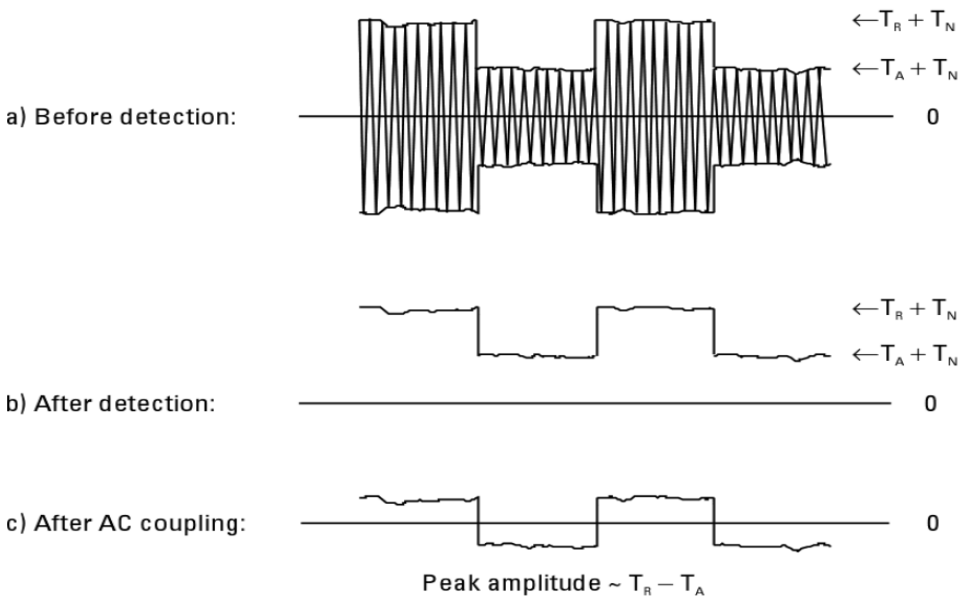

Fig. 6 - Waveforms around the detector of the system [4, p.5]

In Fig. 6, the horizontal axes are time and the vertical axes are the voltage levels. After the filter and A/D converter, the computer records voltage levels which correspond to the difference in brightness of the antenna and the reference. The radiometer is also calibrated in a controlled environment and the computer calculates the approximate physical temperature of the environment based on the voltage data.

CHAPTER THREE

Ice Accretion Sensor

Material Properties of Water and Ice

At microwave frequencies, the difference between liquid water ($\varepsilon_r \approx 80$) and ice ($\varepsilon_r \approx 4$) is easily detectable. This is due to the huge difference in electrical permittivity that the different phases of water possess. The polarizability of liquid water gives it a high electrical permittivity. Polarization refers to the ability of a material's dipoles to interact with an applied electromagnetic field when it is subjected to one [11, p.42]. However, as the water freezes, the state change limits the ability of the molecules to rotate and store energy by aligning with the applied electromagnetic field [12, p. 93].

When both the energy storage and losses are considered, the electrical permittivity of a material is expressed as a complex value. The real part of the permittivity relates to the energy storage capabilities of the material while the imaginary part corresponds to its energy loss capacity. Permittivity is a function of frequency and several models are available to describe that dependence. One such model is the Debye equation.

The Debye model was developed by Peter Debye and is used for estimating the real and imaginary components of the complex permittivity of many different materials. Water is one such material that follows this model. The Debye equation is

$$\dot{\varepsilon}_r(\omega) = \varepsilon_r'(\omega) - j\varepsilon_r''(\omega) = \varepsilon_{r\infty}' + \frac{\varepsilon_{rs}' - \varepsilon_{r\infty}'}{1 + j\omega\tau_e} \qquad (10)$$

In (10), $\varepsilon_r'(\omega)$ is the real part of the permittivity while $\varepsilon_r''(\omega)$ is the imaginary part. ε_{rs}' is the real part of the complex permittivity at zero frequency or DC and $\varepsilon_{r\infty}'$ is the value at

very large (ideally infinity) frequencies. ω is the radian frequency and τ_e is the relaxation time constant. The relaxation time constant is the time it takes the free charge density placed inside a conductor to decay to e^{-1} = 0.368 or 36.8 percent of its initial value [11, p. 56]. Fig. 7 below shows the complex permittivity of water versus frequency at 25℃ and Fig. 8 shows the relaxation spectra of water and ice at 0℃.

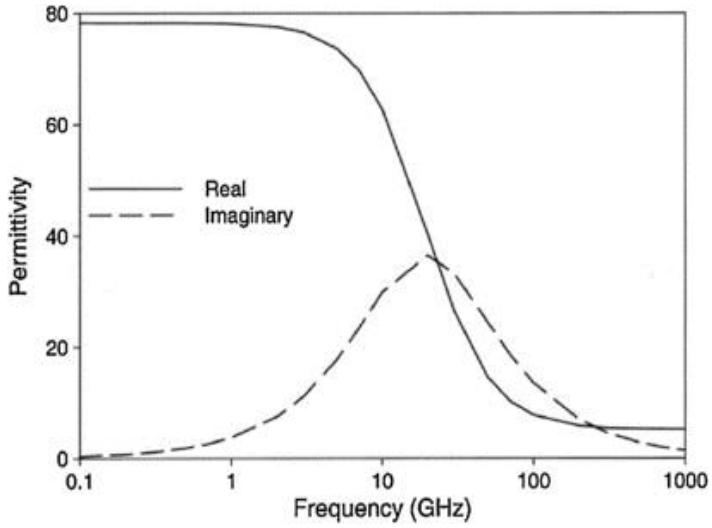

Fig. 7 – Complex permittivity of liquid water versus Frequency [13, p.5]

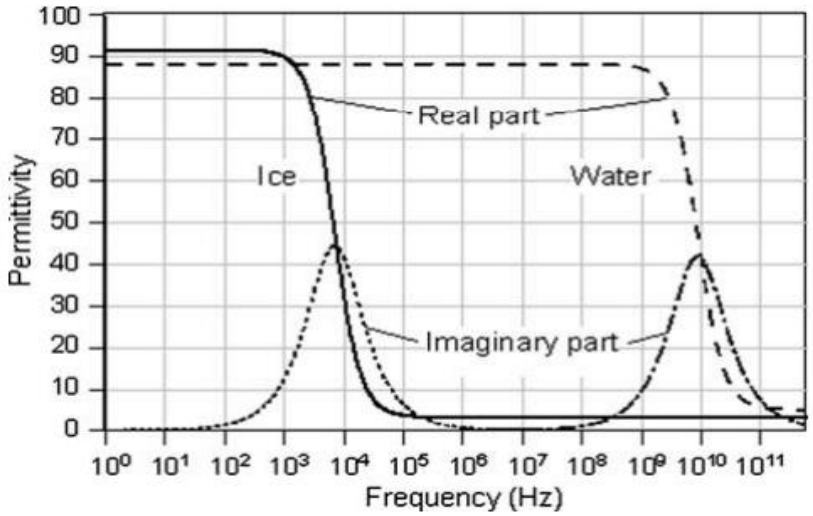

Fig. 8 - Relaxation Spectra of Water and Ice at 0°C [13, p. 5]

Radiometer Antenna Design

The antenna for a system that aims to detect ice accretion in jet engines would ideally need to be a low loss receiving structure. It would also need to feature a large bandwidth which creates the opportunity for the system to acquire sufficient emission data over time and frequencies.

A waveguide-to-coax adapter was initially used as the receiving mechanism at the inception of the project. The use of a waveguide-to-coax adapter eliminated most concerns about dielectric losses. However, the air cavity and bulky size of the waveguide-to-coaxial adapter made it an unviable solution. Even if it were possible to use such a structure, the adapter would need a process seal insert to fill said air cavity. Though this seal might address the engine pressure concerns, it still does not provide a solution for the limited space available for the antenna on the stator vanes of the engine. Figures 9 and 10 below show a waveguide-to-coaxial adapter mounted on a model of the stator vanes and the input reflection coefficient of the feed structure.

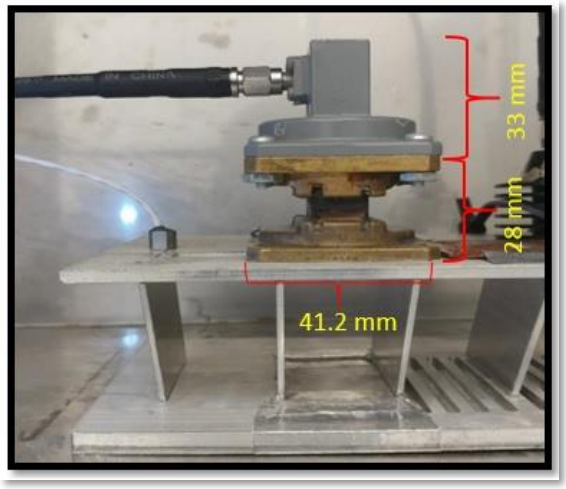

Fig. 9 - Waveguide-to-Coax adapter with process seal insert

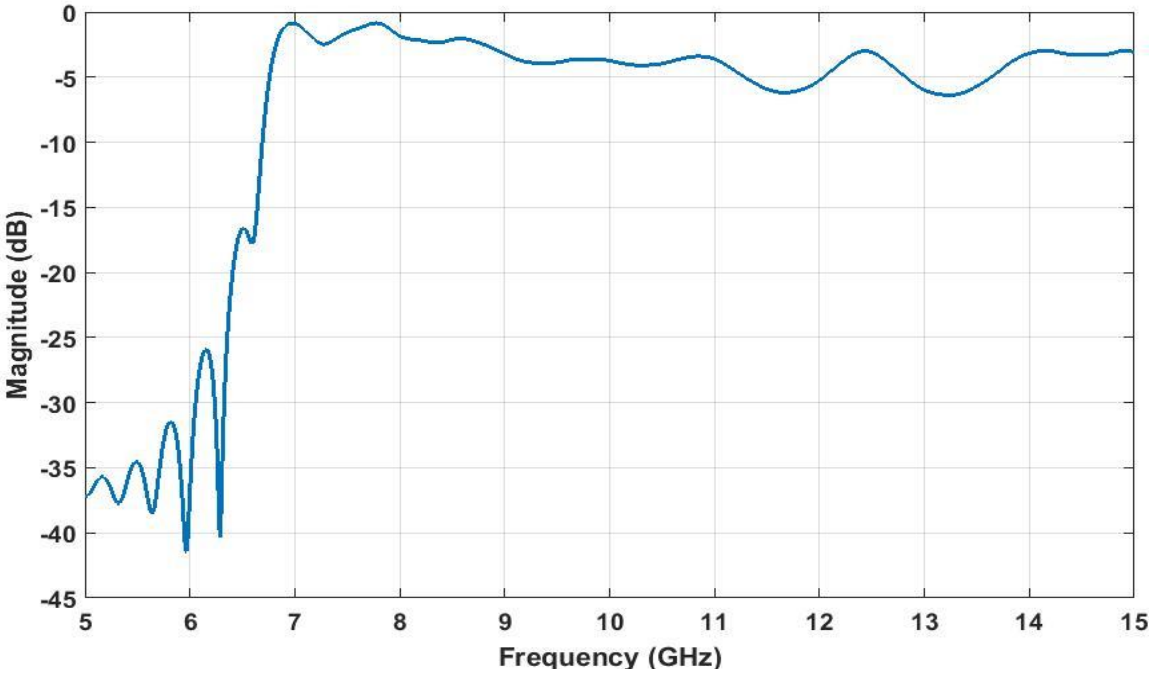

Fig. 10 - S_{21} of the Waveguide-to-Coaxial adapter

Microstrip Antennas

Microstrip antennas are often used for high frequency applications because of the simplicity of their designs and ease of fabrication. They are usually small-scale structures which make their use as an alternative to the waveguide-to-coax adapter advantageous for engine space constraint problems. However, the major disadvantages typical of this type of antenna that had to be addressed are small bandwidth and low radiation efficiency [14, p. 7-2].

A bow-tie and a rectangular patch antenna were initially simulated and tested as potential candidates for the sensor, but these failed to meet the design requirements imposed by our application. Table 1 below shows that the bow-tie design was unable to meet the input return loss requirement in simulation. The patch antenna passed the return loss specification in simulation but, failed when fabricated. For improved thermal

sensitivity, it was agreed that the input return loss be at least 15dB for testing considerations. Table 1 shows a comparison of the results of antenna types analyzed during the project.

Table 1 – Antenna Result Comparison

Antenna	Null Frequency (GHz)	S_{11} Magnitude Null Depth (dB)	Bandwidth (-10dB) (MHz)
Bow-Tie (Modified)	11.15	-10.956	32
Patch (Simulation)	9.94	-25.8	883
Patch (Fabricated)	10.25	-7.89	0

An antenna's bandwidth is commonly considered to be the frequency range for which the S_{11} < -10 dB. Figures 11 through 15 show the simulation model and S_{11} plots of the rectangular patch and bow-tie antennas.

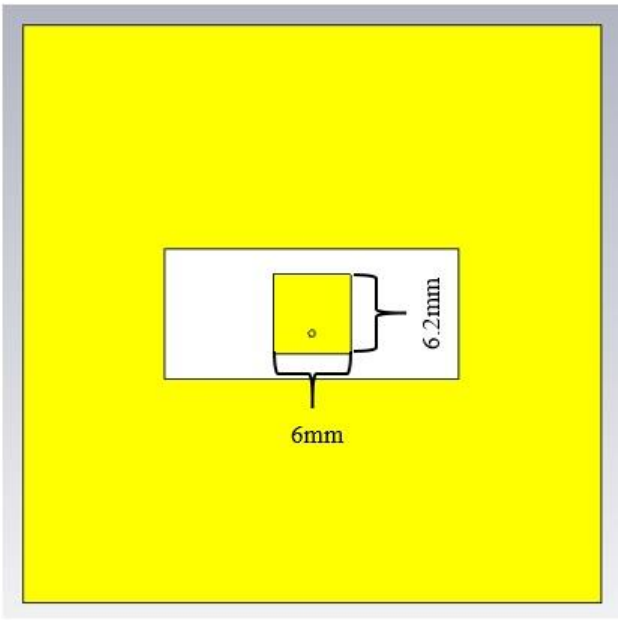

Fig. 11- CST model of the Rectangular Patch Antenna [9, p.35]

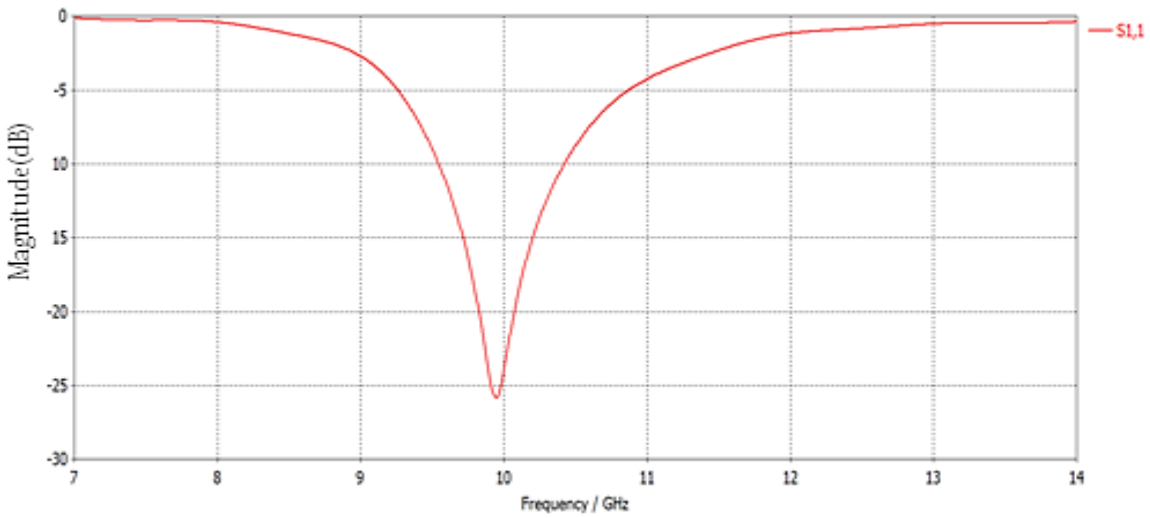

Fig. 12 - S_{11} of the Rectangular Patch Antenna (Simulation)

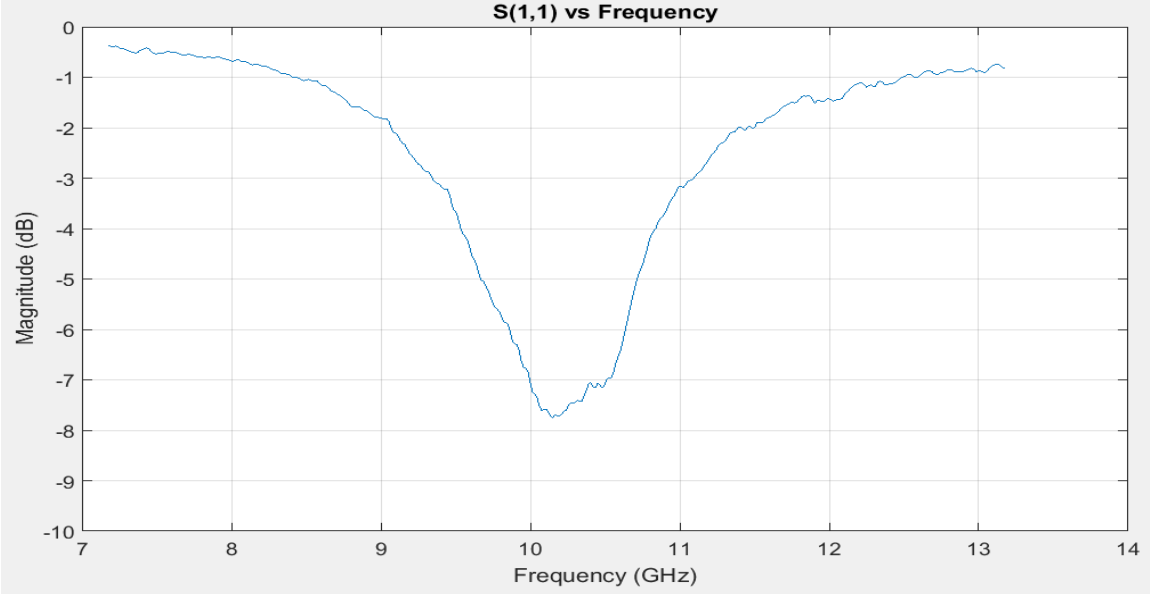

Fig. 13 - S_{11} of the Rectangular Patch Antenna (Fabrication)

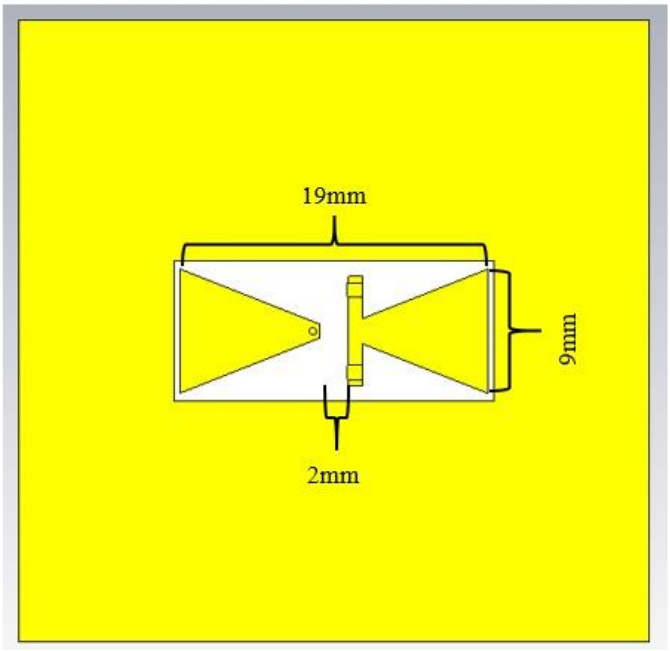

Fig. 14 - CST model of the Bow-Tie Antenna [9, p.35]

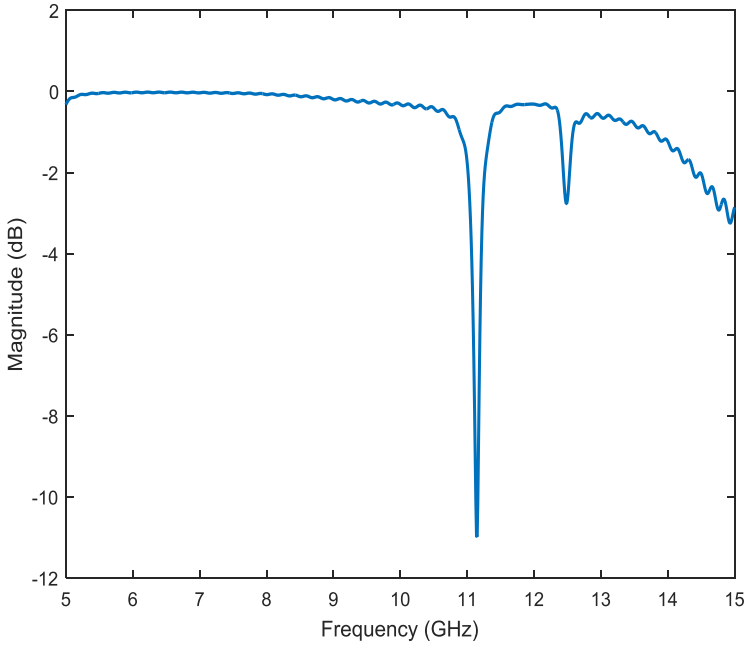

Fig. 15 - S_{11} of the Planar Bow-Tie Antenna

Hybrid Planar Antenna

A hybrid planar antenna was designed based on the rectangular patch and bow-tie antennas and fabricated for use in the radiometer system. The rectangular patch antenna presents the unique advantage of being a narrow-band, wide beam transmitter with a size relatively smaller than the bow-tie antenna. The bow-tie antenna, on the other hand, produces a wider bandwidth than the rectangular patch. The hybrid antenna ideally had to be a small-scale structure capable of producing a wide bandwidth. The antenna also had to fit within the inner dimension of a WR 90 waveguide because of the aperture space on the stator vane model. The inner dimensions of a WR 90 measures 22.86 mm (0.9 in) by 10.16 mm (0.4 in).

Computer designs and simulations were performed using a 3D CAD electromagnetic solver by CST (Computer Simulation Technology). Antenna designs were modeled on a 59 mils thick FR-4 substrate. The thickness was selected as a compromise between bandwidth, antenna loss, and space constraint placed on the design. Though bandwidth of these antenna types increase with substrate thickness and aperture size, so does the loss. FR-4 is a high loss substrate with a dielectric constant of about 4.3. Losses also increase with higher frequencies due to the loss tangent. The loss tangent is the ratio of the imaginary part of the permittivity to the real part and increases with increasing frequency [15, p. 377].

During simulation, a modelled SMA connector with a waveguide port was used to simulate the excitation signal for the antenna. A grounding wall was placed around the antenna to reduce the amount of fields propagating into the substrate. In CST, the grounding wall was modelled as blocks of copper that formed a rectangular fence around

the antenna. With the fabricated antenna, the grounding wall was made of copper wire stitched around the antenna through closely drilled holes spaced at less than half a wavelength based on standard design procedures. The top layer of the board also included a copper layer that surrounded the antenna to mitigate the effects of the antenna impedance change due to physical contact with the stator vanes

The antenna board was fabricated using an LPKF ProtoLaser S machine. Testing of the physical antenna was performed using an Agilent Technologies PNA-L N5230C Network Analyzer that covers a range from 300 kHz to 13.5 GHz. The antenna board was a square that measured 40.86 mm (1.608 in). Figures 16 through 19 show the simulation model and fabricated hybrid planar antenna.

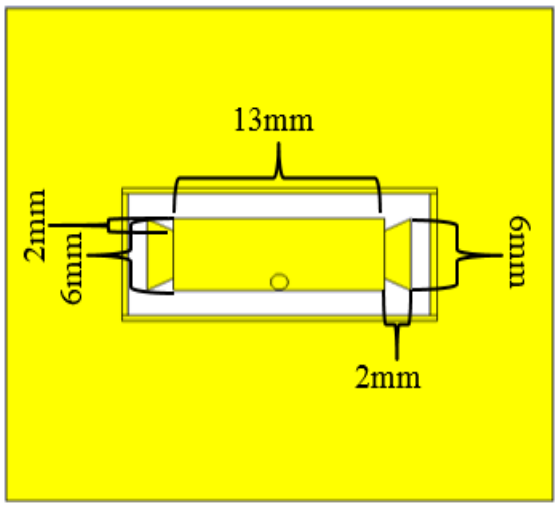

Fig. 16 - Front View of the Simulation Model of the Hybrid Antenna

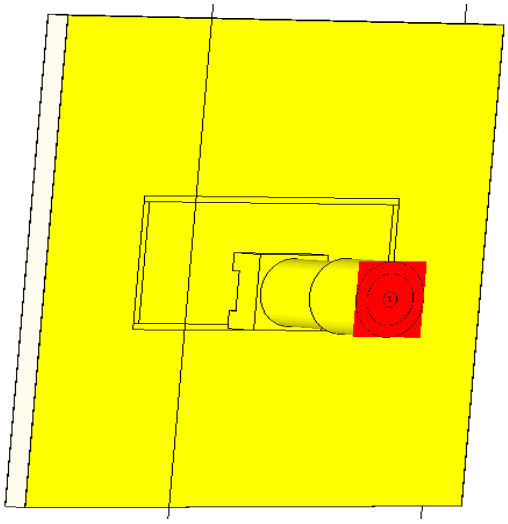

Fig. 17 - Back View of the Simulation Model of the Hybrid Antenna

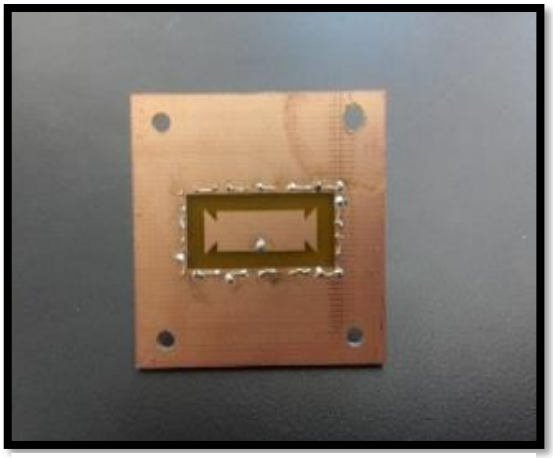

Fig. 18 – Front View of the Fabricated Hybrid Antenna

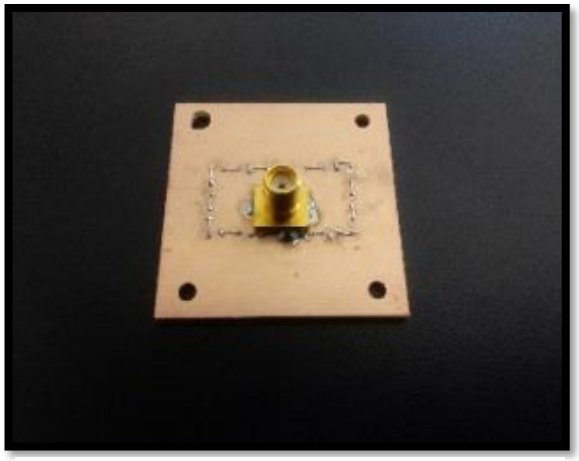

Fig. 19 – Back View of the Fabricated Hybrid Antenna

Fig. 20 shows a plot of the input reflection coefficient of the simulation and that of the fabricated antenna. Both nulls were not as deep as the simulation nulls. The first null was lower in frequency and the second was higher. Differences between the simulation and measurement result are due to material defects from the fabrication process.

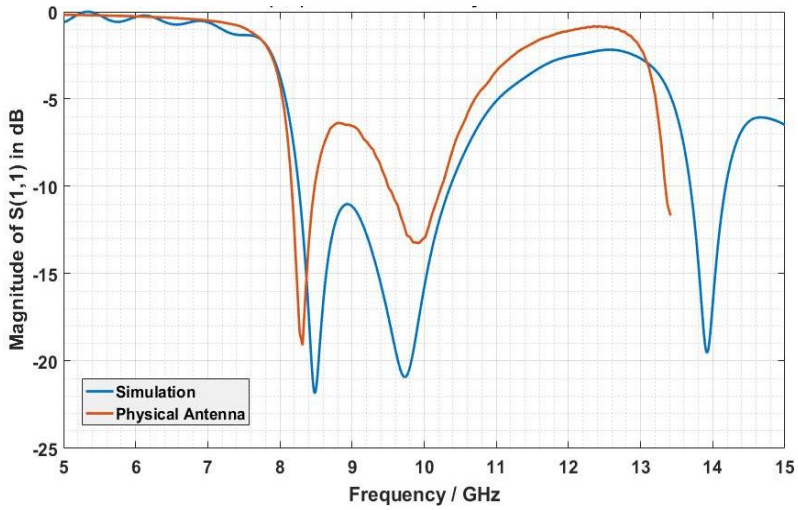

Fig. 20 – S_{11} of the Simulated and Fabricated antenna

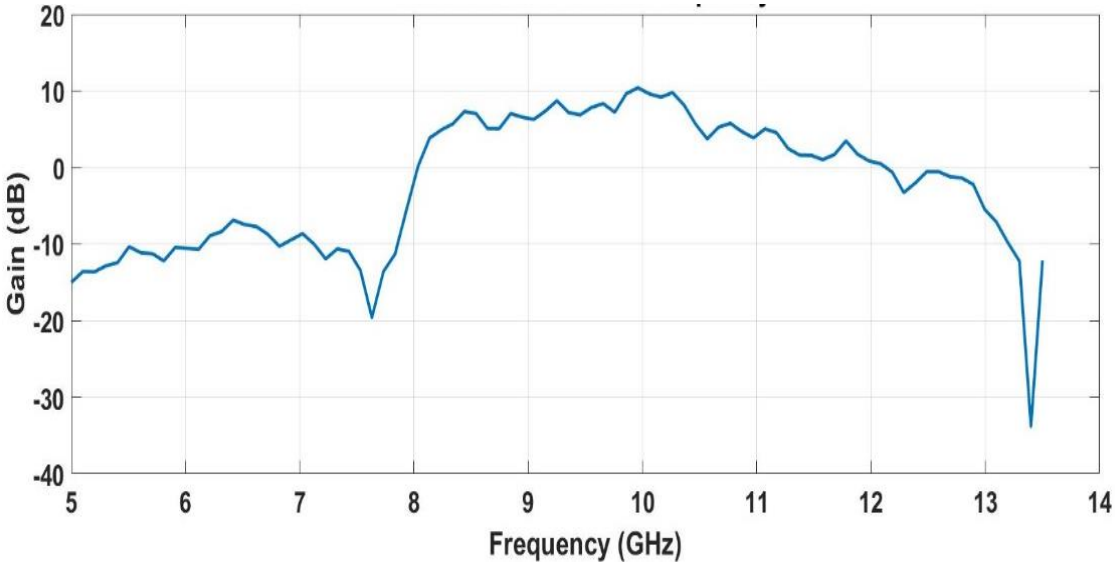

Fig. 21 - Measured gain of the Fabricated Antenna

The gain of the antenna, shown in Fig. 21, was obtained using a second antenna with a known gain, HRN-0118, and with the Friis transmission equation using MATLAB. The simulated azimuth and elevation cuts of the farfield directivity of the antenna is shown in Appendix A.

Achieving low loss was a primary goal of the antenna to prevent its own thermal noise from masking the thermal emissions of the environment. Antenna losses (radiation efficiency < 1) add noise to the antenna's output. Figure 22 shows a simulated total efficiency of 63.3% at 9.7 GHz. Unlike radiation efficiency, total efficiency takes into account losses due to impedance mismatch.

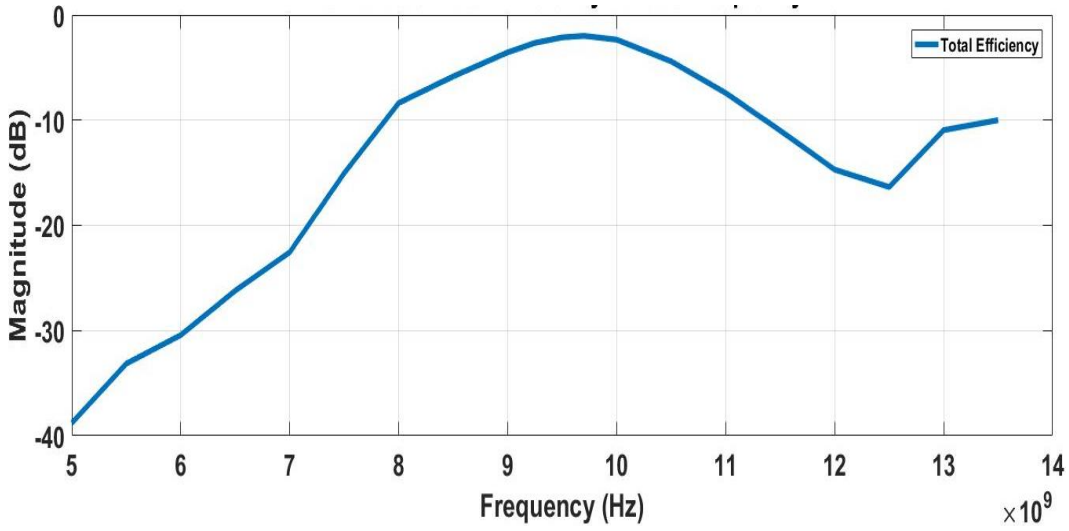

Fig. 22 – Simulated Total Efficiency

Table 2 - Antenna Result for the Hybrid Planar Antenna

Antenna	Null Frequency (GHz)	S_{11} Magnitude Null Depth (dB)	Bandwidth (-10dB) (MHz)
Hybrid (Simulation)	8.45, 9.76	-22.8,-21.97	2000
Hybrid (Fabricated)	8.35, 9.97	-17.6,-13.51	346,685

A second prototype of the antenna was fabricated and used a substrate with a lower dielectric constant. The Rogers RO3003 high-frequency laminate was selected for the design of the second prototype. Table 3 below provides a side-by-side comparison of some of the properties of the RO3003 and FR-4 substrates at 10 GHz.

Table 3 – Comparison of FR-4 and RO3003 Substrates [2, p.37]

Property	FR-4	RO3003
Dielectric Constant	4.3	3.00
Loss Tangent	0.018	0.001
Available Thickness	0.059 in	0.060 in

Table 3 above shows a difference of 1.3 in the dielectric constant values for FR-4 and RO3003. The loss tangent of FR-4 is slightly greater than 10 times that of the RO3003 substrate which makes it an inadequate substrate for microwave radiometers. Figures 23 and 24 below show the S_{11} and gain plots of the second prototype.

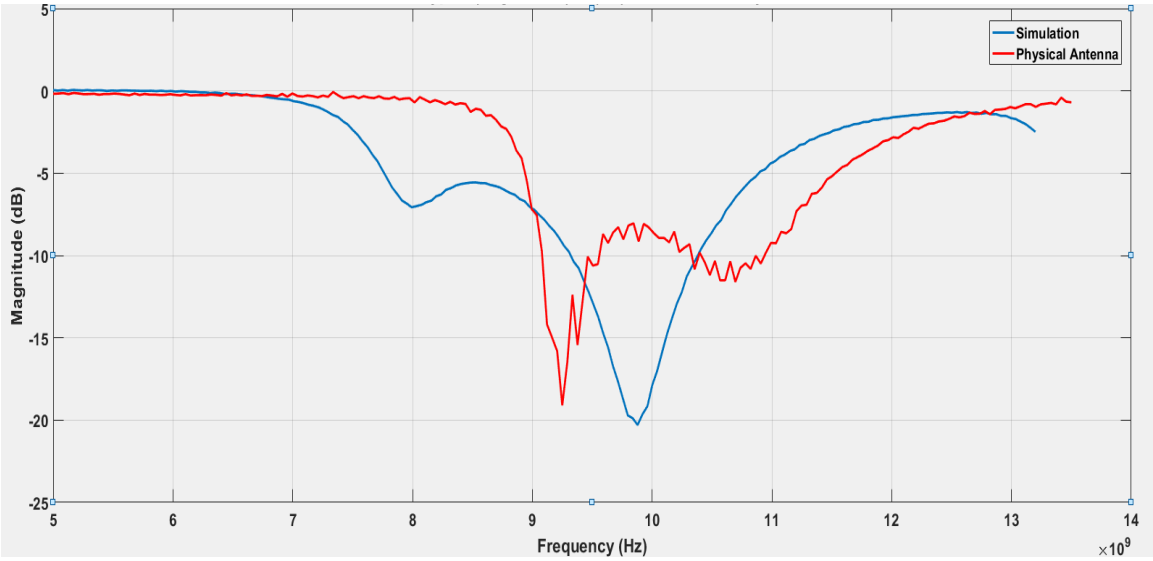

Fig. 23 - S_{11} of the simulated and fabricated antenna (RO3003)

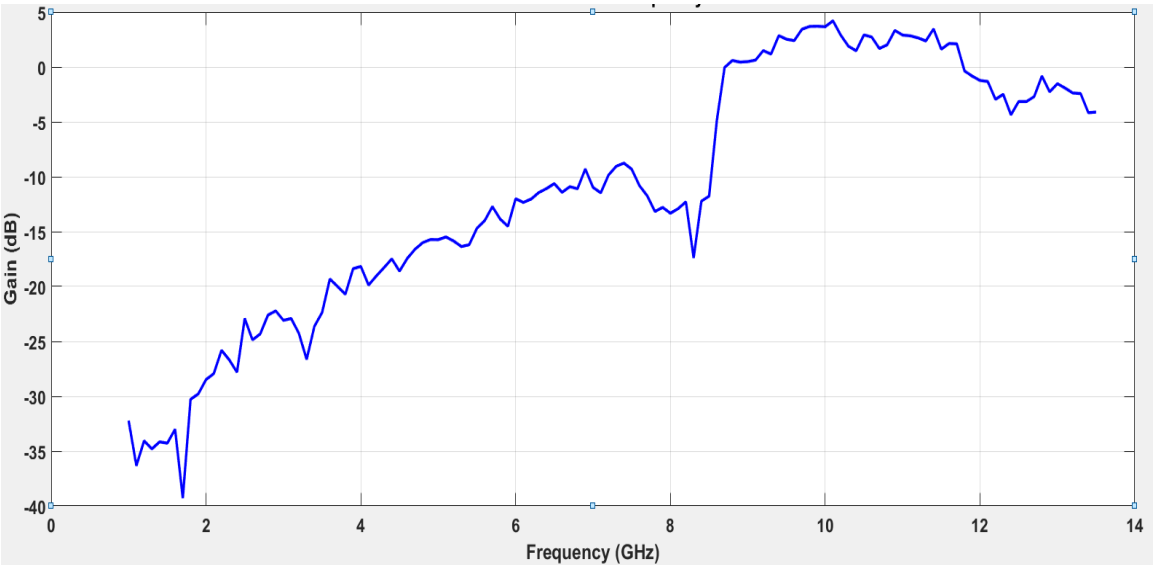

Fig. 24 – Measured gain of the fabricated antenna (RO3003)

A 685 MHz bandwidth was measured around a center frequency of 9.85 GHz and a 346 MHz bandwidth at 8.35 GHz for the first antenna. A bandwidth of 507 MHz was measured at a center frequency of 9.24 GHz and a 780 MHz bandwidth at 11.72 GHz for the second prototype. The maximum gain of the first prototype was 10.41 dB at 9.6 GHz, while the second prototype produced a gain of 4.207 dB at 10.1 GHz.

Before arriving at the final design and characterization, a number of other designs were simulated. Those results are shown in Appendix B. A number of parametric sweeps varying the different lengths and widths of the final design were taken to classify its frequency response. Figures 25 and 26 show the different parameters swept and the result of the antenna width sweep. Appendix C contains the results of the other sweeps.

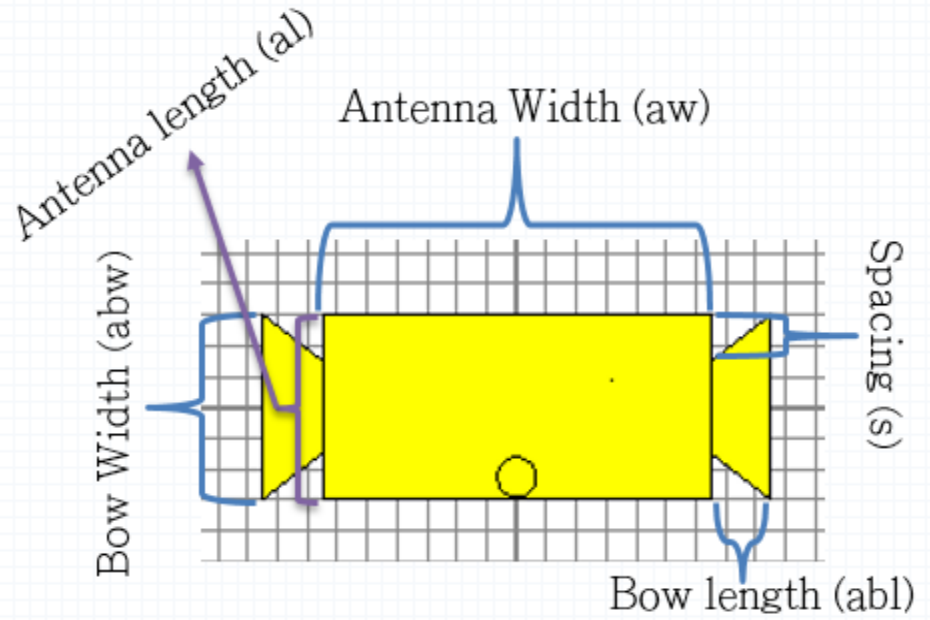

Fig. 25 – Antenna Parameters

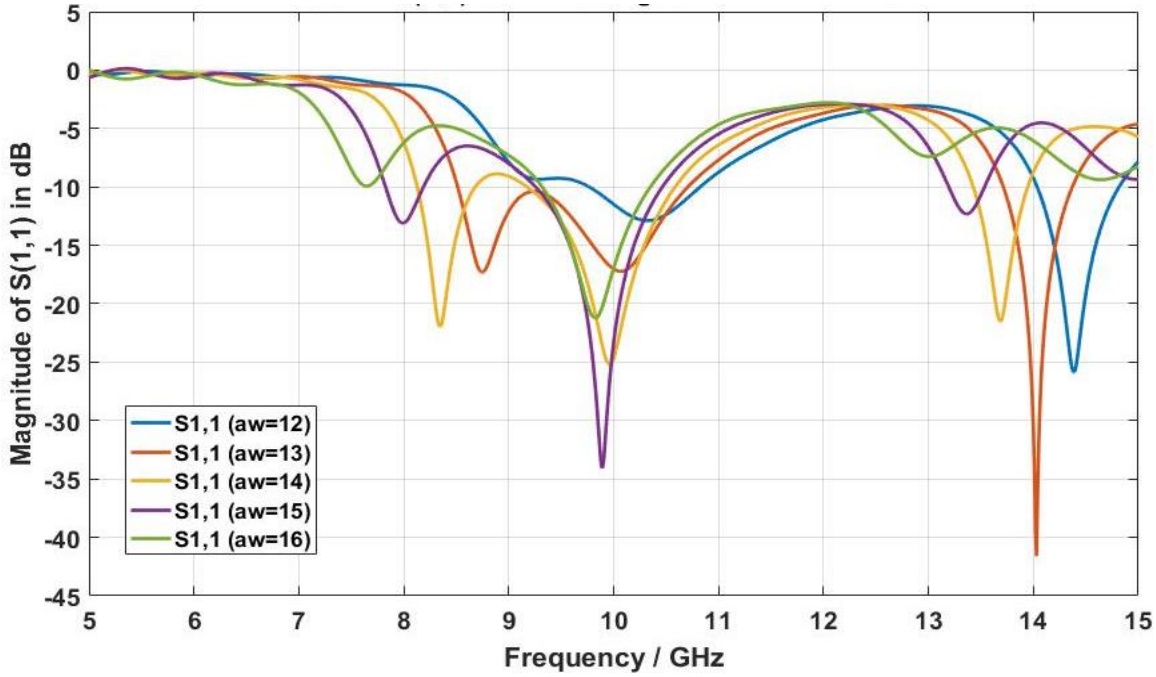

Fig. 26 – Parametric sweep of the Antenna's Width

Before the antenna can be mounted to the stator vanes of an engine and used for testing, a low loss dielectric layer would need to be placed over the antenna for durability. This layer would need to be resilient to withstand extreme flight temperatures and durable enough to withstand high engine pressures. The dielectric layer might slightly change the frequency response characteristics of the antenna, but would not affect its ability to pick up the noise of the environment.

CHAPTER FOUR

Experimental Results of the Ice Accretion Sensor

The following section shows data from in-lab testing of the ice accretion sensor. The goal of the lab tests was to investigate the performance of the sensor in an environment that closely approximated the real-world measurement environment. The temperature and geometry of the test-setup were similar to what would be experienced in a jet engine for the ice accretion sensor.

Test Set-Up

Ice Accretion Sensor

The major components of the ice accretion sensor are shown in Fig. 27.

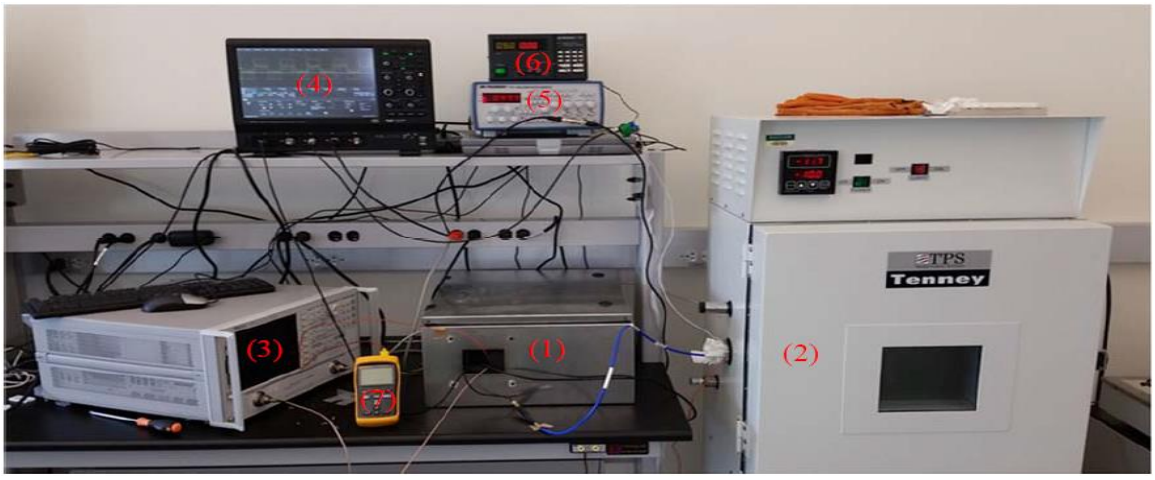

Fig. 27 – Test set-up of the ice accretion sensor. Items numbered for identification [9, p. 40]

In Fig. 27, the component labelled (1) is the microwave radiometer. It was first develop in 2006 by Laura R. Ballew. The radiometer was placed inside an insulated

stainless steel box and included polymer foam sheets for temperature stability [16]. The reference load was placed inside the box during experiments and had to be at a stable temperature. Temperature fluctuations of the reference load can cause data inconsistencies. The heat dissipated from the internal components was enough to warm the box to approximately 36°C. At times, a heat gun was used to quickly warm up and maintain the temperature [2].

The component labelled (2) is the Tenney environmental test chamber (ETC). It hosted the radiometer antenna, and sometimes, the reference load. The temperature range of the ETC is from -77 °C to 150 °C which is adequate enough to convert liquid water to ice and back to the previous state. Test runs were over a temperature range of 10 °C to -10 °C for creating ice and returning it to its liquid state.

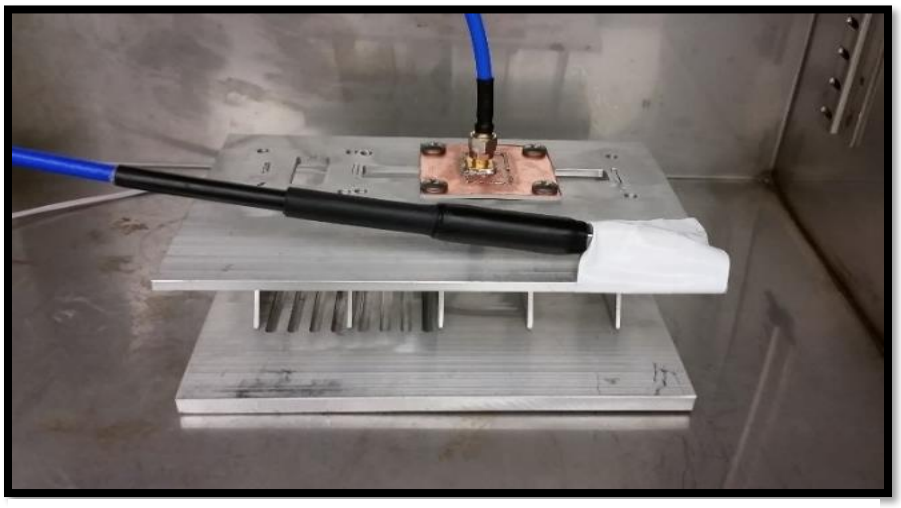

Fig. 28 – Antenna mounted on Stator Vanes in the ETC

Fig. 28 shows the antenna mounted to the stator vanes and the reference load taped for thermal contact. A webcam was also placed inside the ETC to capture pictures with each data acquisition for processing.

The component labelled (3) is the HP-8720ET VNA used as the local oscillator (LO) for the radiometer. The output of the LO was connected to the frequency mixer located within the enclosure of the radiometer. The component labelled (4) is the LeCroy HDO4508 oscilloscope that receives the inputs of the radiometer, resistance temperature detector (RTD) probe, and a function generator that is shown in figure above and labelled (5). The oscilloscope displayed the performance of the radiometer and served as a visual confirmation.

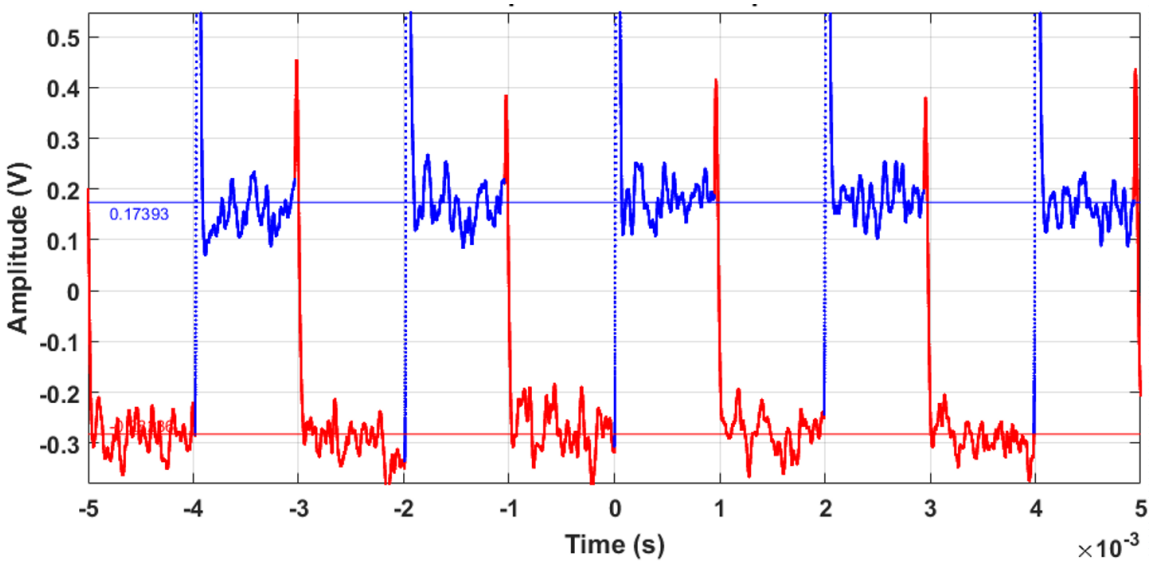

Fig. 29 – Example of the radiometer output for a single data capture displayed on the Oscilloscope

The data displayed in Fig. 29 above is an average of 100 sweeeps of the oscilloscope. The blue trace represents the output voltage level of the reference load and the red trace represents the output voltage level of the antenna. The positive and negative results are due to capacitive coupling which filters out the DC components of the signal and increases the resolution of the signal measurements. The time window for a single sweep from the oscilloscope was 10 ms. The oscilloscope captured five voltages from the

reference load and antenna with the 500 Hz switching frequency of the Dicke switch. The results were time-stamped and paired with the corresponing temperature within the ETC. Data acquisition time for the output shown in Fig. 30 was 20 seconds [2].

The DC power supply is labelled (6) in Fig. 28 and provided the resistance temperature detector proble with 5V. Temperature data from the RTD was also averaged like the output of the radiometer. Lastly, component (7) is the Fluke 52 II digital thermometer with a probe that was connected to the reference load. Data from the thermometer was used to check the stability of the temperature of the reference load [2].

Results

During testing, the antenna was mounted on stator vanes of a jet engine compressor design model and placed in an ETC. A dry run was used to determine the level of the background noise of the vanes and to set a reference. Test runs involving 3 mL and 5 mL of distilled water were used to test the sensor. Experiments ran for 80 minutes. During water-based testing, liquids were added after 10 minutes and temperature was dropped to -10 ℃ after 20 minutes to allow the water to freeze. After 50 minutes, the temperature of the ETC was raised to 10℃ and the ice returned to its liquid state. Figures 30, 31, and 32 below compare measurement results from tests using a waveguide-to-coax adapter, a rectangular patch antenna, and the hybrid antenna.

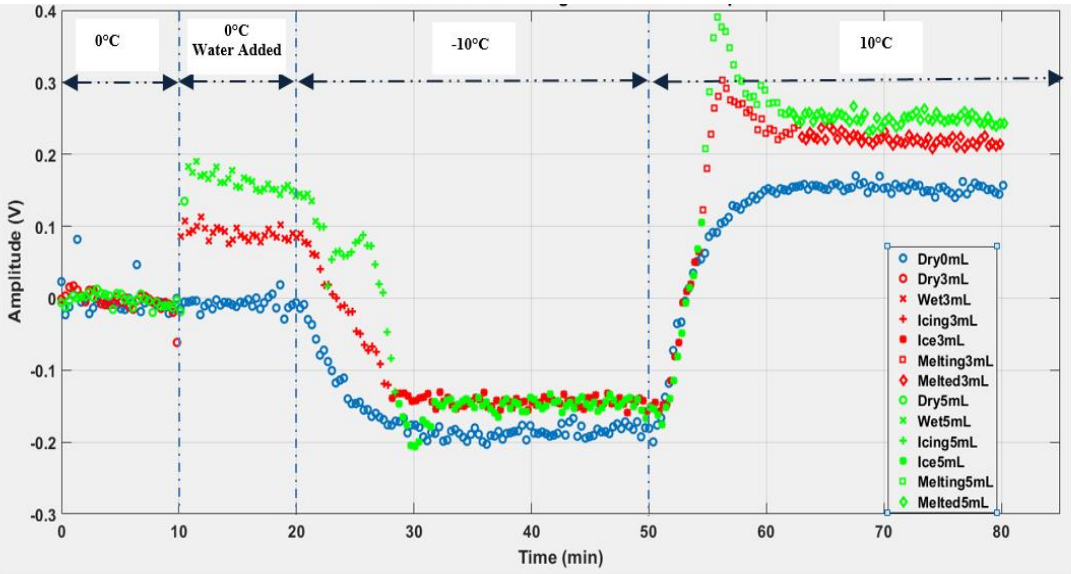

Fig. 30 - Measurement with the Waveguide-to-Coaxial Adapter

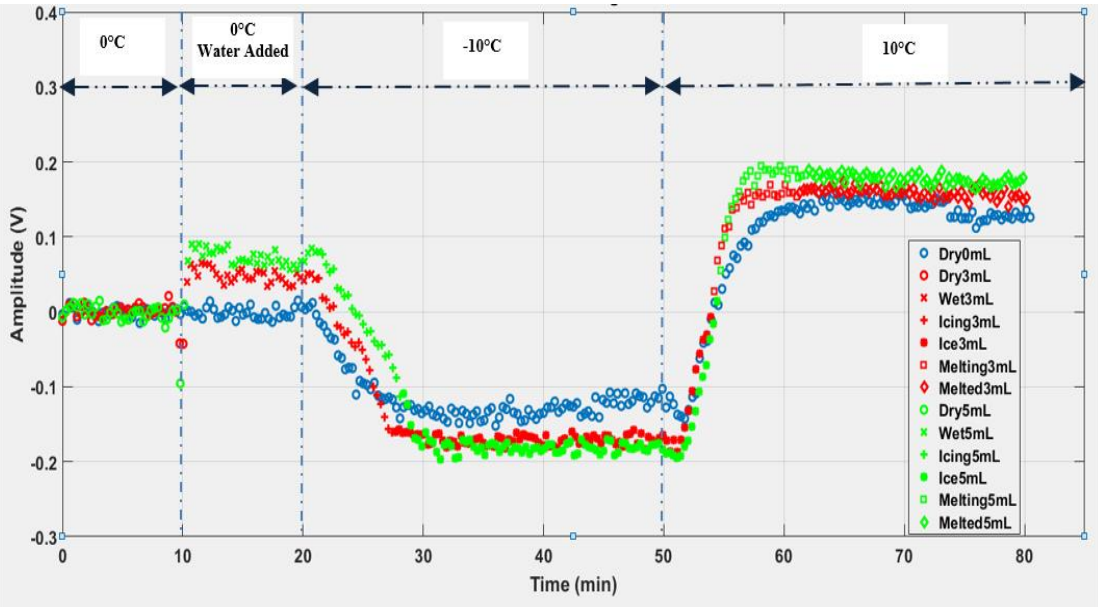

Fig. 31 - Measurement with the Rectangular Patch Antenna

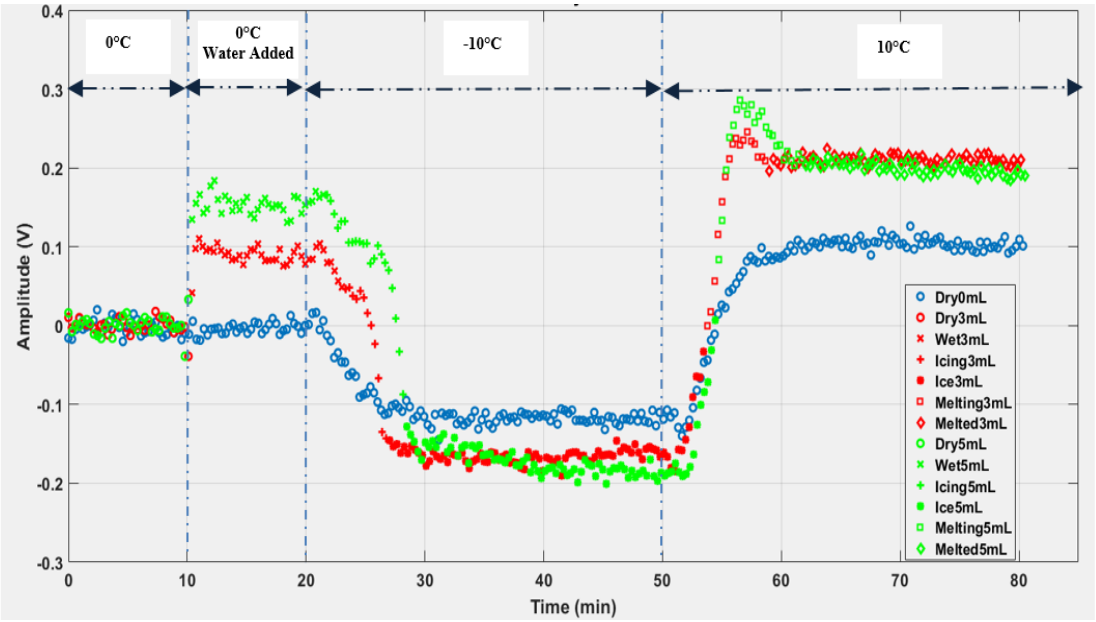

Fig. 32 - Measurement with the Hybrid Planar Antenna

The highest resolution is seen with the waveguide-to-coaxial adapter and the lowest with the rectangular patch. As opposed to the rectangular patch, the distinction of dry, wet, and iced vanes are more clearly distinguishable with the hybrid planar antenna. The different volumes of water are no longer differentiable when frozen due to vibrations of the ETC that cause the water to spread out when the compressor cycles on. This produced a similar brightness for both volumes due to the limited receiving angle of the antenna. The larger voltage amplitude spread of the data and higher resolution with the hybrid antenna speaks to an improved sensitivity compared to the patch antenna.

The results presented above demonstrate the ability of the microwave radiometer system to detect ice using the hybrid planar antenna. The antenna had about twice the resolution when detecting water and maintained its higher sensitivity compared to the rectangular patch antenna.

CHAPTER FIVE

Interferometry

Interferometry refers to a group of measurement techniques in which two signals, usually electromagnetic waves, are merged to create an interference pattern. This interference pattern is then measured and analyzed for the extraction of information from the object or environment under test. Interferometers provide highly sensitive measurements that are typically not possible using other techniques. For example, three interferometers are used as a part of the LIGO (The laser interferometer gravitational-wave) observatory to detect gravitational waves from space [17].

Interferometers work because of the unique properties of waves. Electromagnetic waves propagate due to the interaction of the electric and magnetic fields which synchronically oscillate. The electric field at any point along the wave propagating in any direction can be described based on the below scalar equation:

$$E(x, y, z, t) = \mathrm{a} \cdot \cos\left[2\pi\left(ft - \frac{z}{\lambda}\right)\right] \tag{11}$$

In (11), **a** is the amplitude of the wave, $\boldsymbol{t}$ is travelling time, $\boldsymbol{f}$ is the frequency, and λ is its wavelength. The phase of the wave is the term in square brackets and varies based on both time and displacement along the axis under consideration [18, p.4].

As time elapses, a point of constant phase of the wave-front travels a certain distance along the propagating axis with a velocity,v, shown in the below equation:

$$v = f \cdot \lambda, \tag{12}$$

In free space, the wave travels at its maximum velocity, $v = c$. This speed is based on the permittivity and permeability values of free space and is not realizable in real world experiments. The permittivity of a material is a proportionality constant that relates the electric field intensity and the electric field displacement. Permeability, on the other hand, is a constant of proportionality that is a measure of a material's ability to resist the forming of a magnetic field. The speed of light in vacuum is calculated based on the formula below:

$$v = c = \frac{1}{\sqrt{\varepsilon_0 \mu_0}}, \tag{13}$$

where ε_0 is the permittivity and μ_0 is the permeability of free space.

To incorporate other variables that are not considered in free space experimentations, relative values of permittivity are defined based on absolute permittivity. Absolute permittivity (ε) is the product of the relative permittivity of a material and that of the permittivity of vacuum. Relative permittivity is often referred to as the "dielectric constant" of the material.

$$\varepsilon = \varepsilon_r \varepsilon_0 , \tag{14}$$

In (4), ε_r is the relative permittivity.

Based on the concepts introduced above, it is easy to discern that the velocity at which a wave through a medium varies based on the dielectric constant of the material.

$$v = \frac{1}{\sqrt{\mu_0 \varepsilon_r \varepsilon_0}} = \frac{1}{\sqrt{\mu_0 \varepsilon}}, \tag{15}$$

Therefore, the higher the dielectric constant of a material, the slower the speed of the propagating wave through it.

A change in velocity is not the only effect that a wave experiences as it travels through different mediums. As a wave travels through different mediums, it encounters

different impendences and reflections are produced. The impedance of an object is a measure of its opposition to the flow of electric current, and it takes into account the combined effects of the object's resistance and reactance [19, p.90]. The intrinsic impedance of an object, denoted by Z, is given by

$$Z = \sqrt{\frac{\mu}{\varepsilon}} \tag{16}$$

Reflections affect a propagating wave in a number of ways, but most significantly for the purposes of this research, is its reduction in the magnitude, the mismatch caused at boundaries and the change in phase of the wave.

At a boundary where there exists a change in impedance, the travelling wave and the reflected wave interfere and produce a standing wave. The standing wave caries the same frequency as the travelling and reflected waves, but with a different phase offset due to the change in phase of the reflected wave [19, p.86 - 88]. Fig. 33 shows a plane wave reflection at an arbitrary boundary of a random medium:

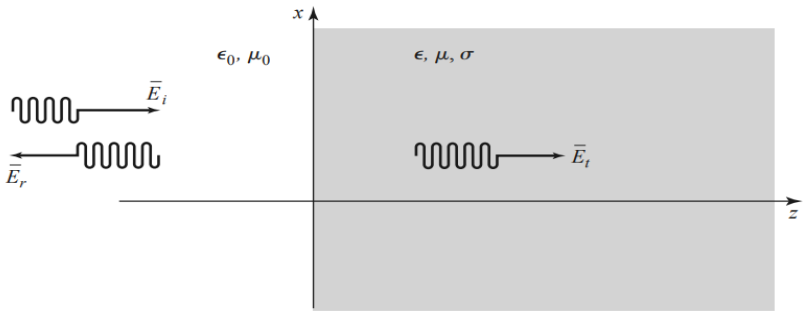

Fig. 33 - Plane Wave Reflection [20]

In Fig. 33, $\bar{E}_i$ is the incident wave, $\bar{E}_r$ is the reflected wave and $\bar{E}_t$ is the transmitted wave. Transmitted waves travelling through interferometer sensor paths are merged and the interference is investigated.

When two waves are superposed, they undergo either a constructive or destructive interference. When the crests and troughs of two interfering waves meet, the amplitudes of the individual waves add together, and this is known as constructive interference. When the opposite happens, the waves experience a destructive inference and the amplitudes subtract from one another. Figure 34 below show a constructive and destructive interference pattern.

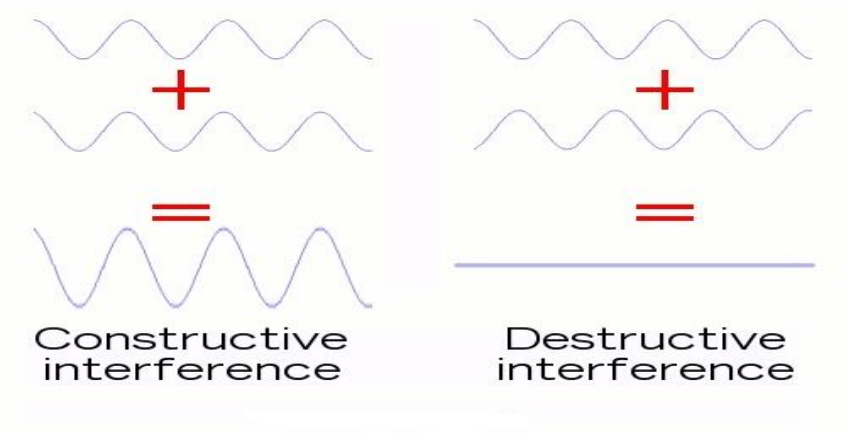

Fig. 34 – Interference Pattern [17]

Mach-Zehnder Interferometer

A special type interferometer, called a Mach-Zehnder interferometer, was used for this project and it involves the splitting of a wave from a single source along two separate paths. One path is exposed to the environment, while the other is not. The path exposed to the environment is called the measurement arm, while the path not exposed is called the reference arm.

An attenuator is usually added to the reference path of the interferometer to adjust the amplitude of the wave to produce a better interference pattern. The change experienced by the wave as it crosses the mensuration section along the measurement

path causes a change in the magnitude and phase of the wave. This change usually produces a different propagating speed that affects the interference from both paths. The attenuator adjusts the amplitude of the wave along the reference path so that the waves along both paths can subtract to zero. Nulls are produced at points where the peaks and troughs of the waves coincide and the opposite otherwise.

Fig. 35 shows an example of shifts in the resulting signal strength for different reflection coefficient values. The values used were 0.9 (which produced the deepest null), 0.7, 0.5, 0.3 and 0.1 (which produced the shallowest troughs).

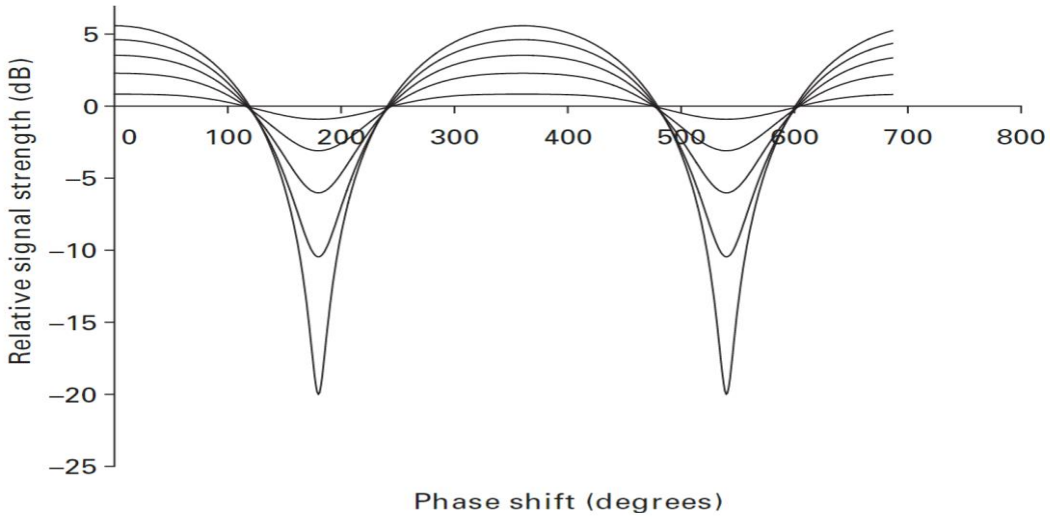

Fig. 35 – Relative Signal Strength versus Phase Shift

Deeper null levels correspond to higher sensitivity since they correspond to a specific frequency or smaller range of frequencies. As the environment under test changes, so do the properties (frequency, magnitude and phase) of the null(s) being observed. Based on frequency shifts and variations in the magnitude and phase of the signals, very precise measurements are made possible using the processes of interferometry.

CHAPTER SIX

Ice Cloud Sensing and Humidity Measurement

Work is on-going for the development of an ice cloud sensor and a high accuracy humidity sensor. The sensor uses techniques of interferometry because of the demonstrated sensitivity and accuracy of a microwave interferometer to detect small environmental changes [12]. The sensitivity required for making ice detection measurement needs to be high due to the small volume fraction of ice crystals. In his paper titled “A microwave frequency sensor for steam quality”, Jean demonstrates the ability of an instrument using an interferometer technique based upon differential lengths to sense a change in the permittivity of steam [21]. A technique capable of detecting changes in steam quality possesses the sensitivity to detect ice clouds and measure humidity.

Ice Cloud Sensor

A simple experiment to determine the sensitivity of the ice cloud sensor was performed by the Microwave Applied Metrology Lab at Baylor University using a Magic Tee Coupler. The team was able to measure a 470 KHz shift in frequency from the addition of a 0.7 mm thick pencil lead place within the measurement section of the magic Tee coupler. The Magic T is a four-port, 180 degree hybrid power divider that is realized using a waveguide. Fig. 36 shows a simulation model of the Magic Tee Coupler. Fig. 37 shows the pencil lead in the measurement arm of the coupler and Fig. 38 shows the observed frequency shift.

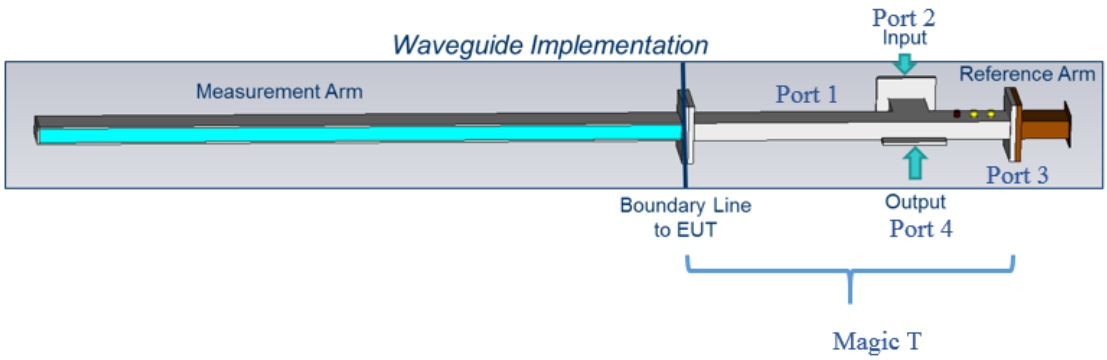

Fig. 36 – Simulation model of the Magic Tee Setup

Due to the geometry of the coupler, a wave introduced into port 2 will divide equally along the paths of ports 1 and 3, but not couple to port 4. Conversely, a wave launched into port 4 will divide between arms 1 and 3, but not couple to port 2 [22, pg. 560]. An Agilent Technologies PNA-L N5230C Network Analyzer provided the input signal and recorded the results.

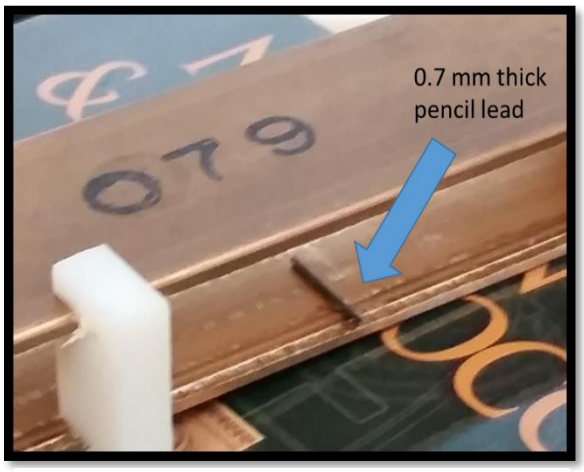

Fig. 38 – Pencil lead in Measurement Arm

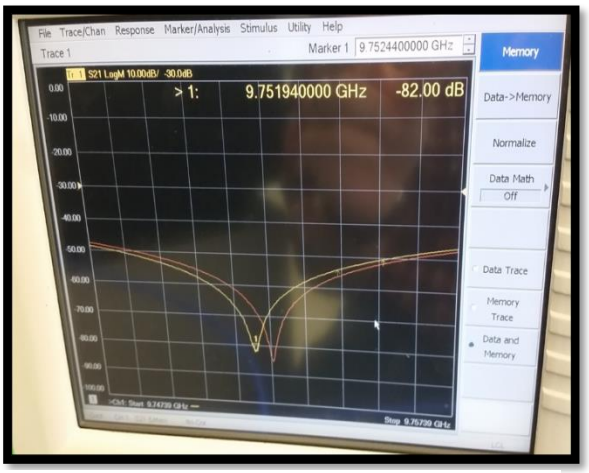

Fig. 37 – Observed Frequency Shift

Jean (12) further validated the sensitivity capability of the ice cloud sensor using simulations performed with the CST Microwave Studio Software. Using foams with slightly different permittivities, he was able to clearly observe shifts in null frequencies.

Table 3 below shows the effective permittivity values of the materials tested and the resulting frequency shifts are shown in Fig. 39.

Table 4 – Effective Permittivity Values

Material	Density (kg/m^3)	Foam Permittivity	Effective Permittivity
Air	1.225	1.000536	1.000536
FR-3704	64.0739	1.045	1.001462
FR-4305	80.0923	1.05	1.001565
FR-3706	96.1108	1.055	1.001668
FR-4310	160.1846	1.07	1.001974
FR-4315	240.2770	1.105	1.002682

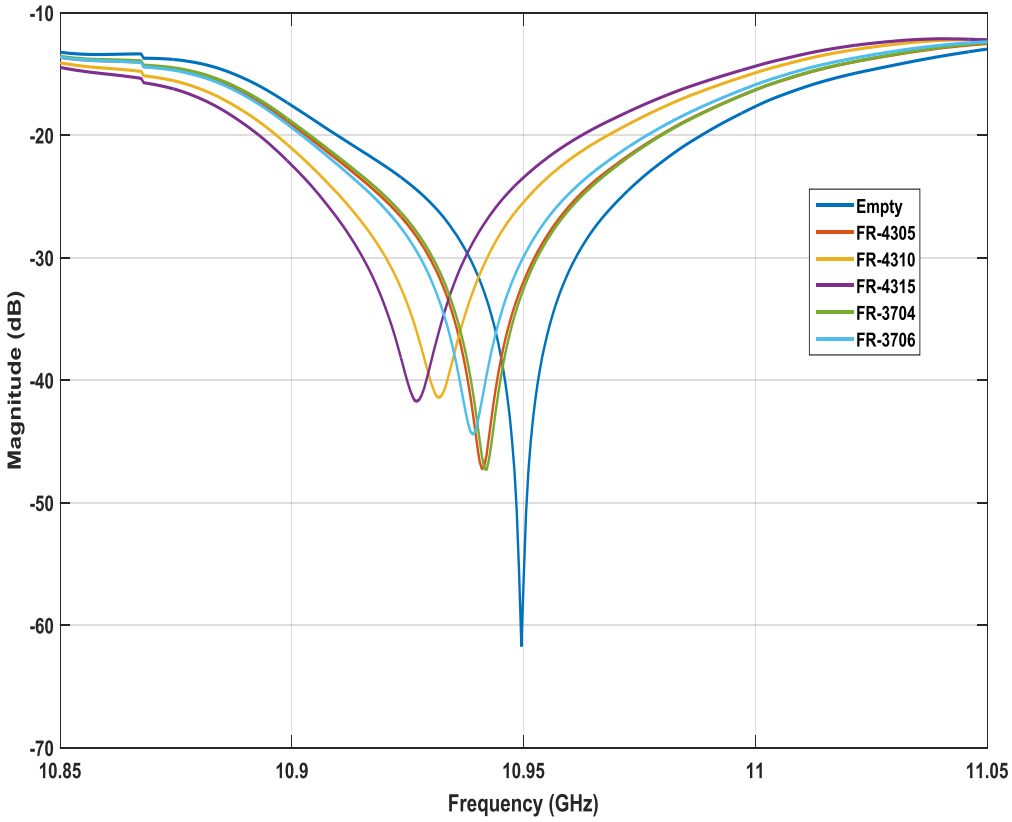

Fig. 39 - Simulated Responses of the Interferometer [12]

The interferometer sensor tests, described in the next chapter, were performed using the Liquid Film and Cloud Tunnel (LFACT) at Baylor University. The LFACT is capable of producing water-based clouds using a marine rated motor and low concentrations of water. Figures 40 and 41 shows the design elements of the LFACT, the position of the test section and mounting of the Magic Tee within the test section.

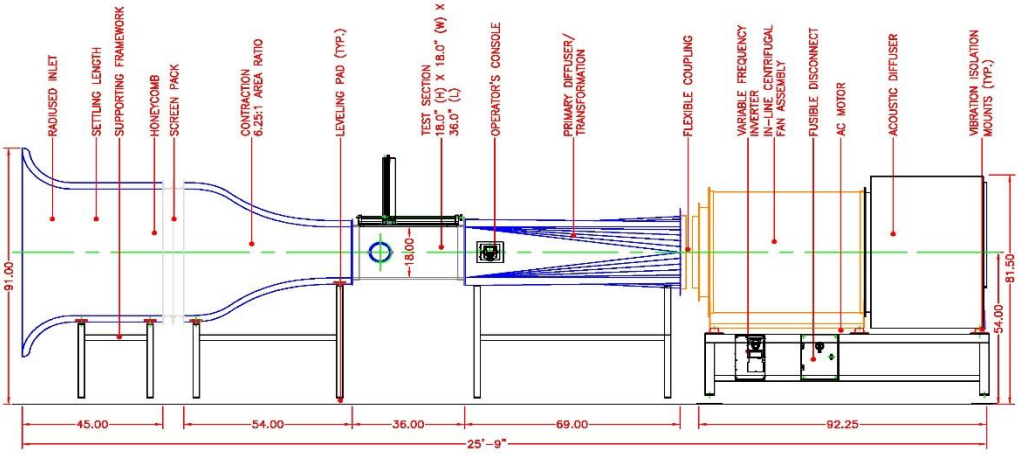

Fig. 41 - Design elements of the LFACT [12]

Fig. 40 - Side view (Left) and front view (Right) of the Magic Tee in the LFACT

Linear regression of test runs with the LFACT using null frequency showed that the sensor was highly sensitivitive to changes in the humidity of the room. The calibrated response of the interferometer sensor over that range of relative humidity shows an adjusted R^2 value of 0.796, with a standard error of 0.752%RH [12]. This discovery presented a second application for the sensor. Fig. 42 shows the interferometer sensor response to changes in humidity.

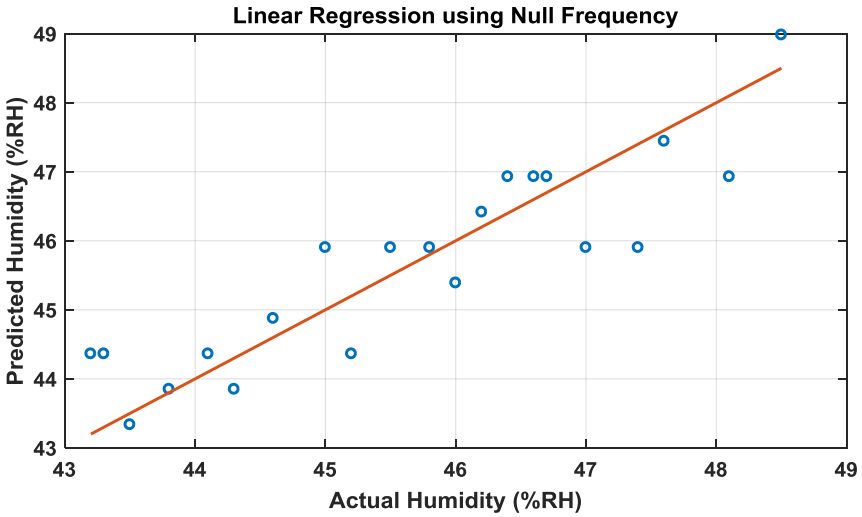

Fig. 42 - Interferometer sensor response to changes in humidity [12]

Humidity Sensor

A planar version of the interferometer sensor was designed for humidity sensing. A planar design presented the advantage of being a small scale, low cost structure that could easily be fabricated. Moreover, it was a design that was easy to model and test in the lab.

For the splitting of the source signal along the reference and measurement paths, two wilkinson power dividers/combiners were used for low frequency testing (<3.5 GHz)

and Weinschel 93459 Model 1515 splitters/combiners were used for higher frequency (6 – 12 GHz). The wilkinson power divider is a 3-dB divider with an equal phase output that is obtained by transforming two 50-Ω loads to 100-Ω and connecting them in parallel to a 50-Ω input line. The output is divided equally and isolated at the design frequency when the output ports are bridged with a l00-Ω resistor [23, p. 331]. Fig. 43 shows the microstrip implementation and performance of the coupler.

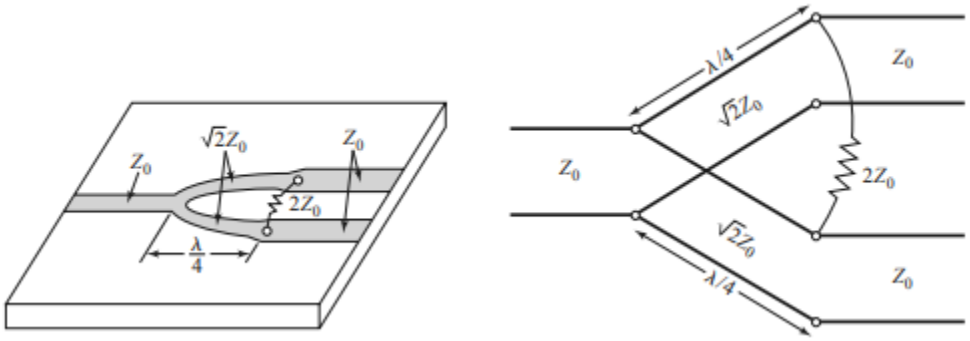

Fig. 43 – Microstrip implementation of the Wilkinson Coupler [23]

The input port sees an impendance of 50-Ω when the parallel ports are terminated in the same impedance [23]. The characteristic impedance of the $\frac{\lambda}{4}$ wave line and resistor value is selected by the following formulas:

$$Z_c = \sqrt{2}(Z_o) = \sqrt{2}(100) = 70.7\Omega \quad (18)$$

$$R = 2(Z_o) = 2(50) = 100\Omega \quad (19)$$

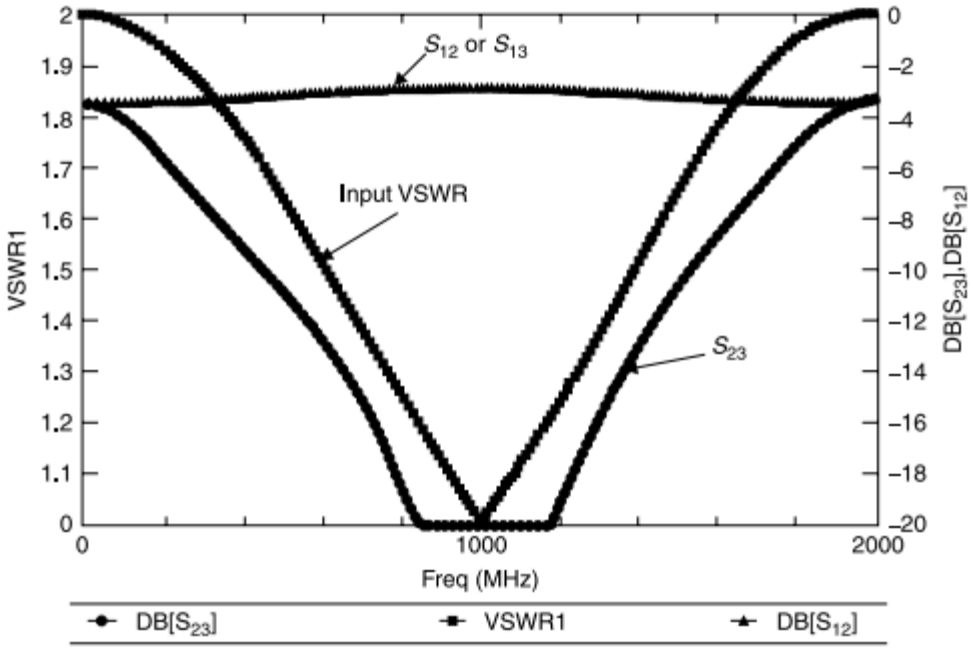

Fig. 44 – Performance of the Wilkinson Coupler [23]

The CST Microwave Studio software was used to design the wilkinson power dividers. Line widths were calculated using LineCalc in ADS and the transmission line lengths were optimized using parametric sweeps in CST for improved perfomance. The simulation model and fabricated board as well as the measured performace of the Wilkinson power divider/combiner is shown in Figures 45, 46, and 47 respectively.

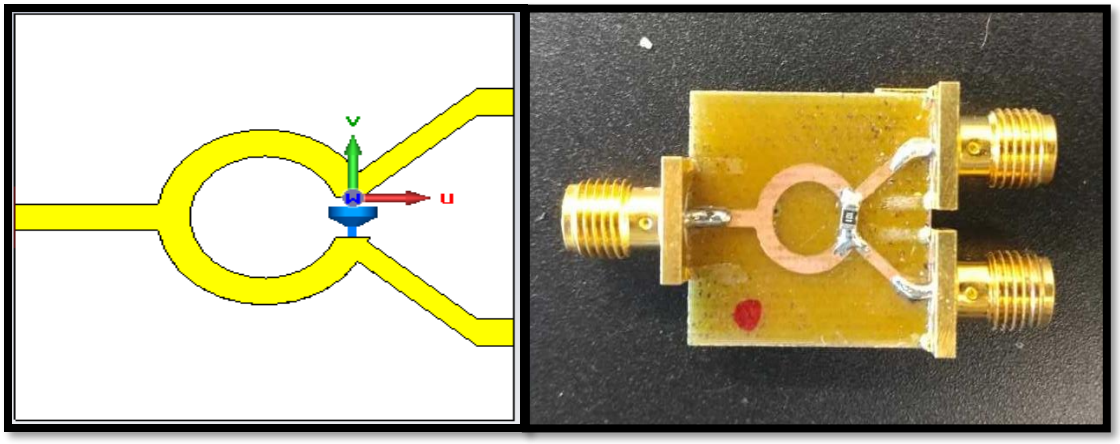

Fig. 46 - Simulation model and fabricated board of the Wilkinson Power Divider

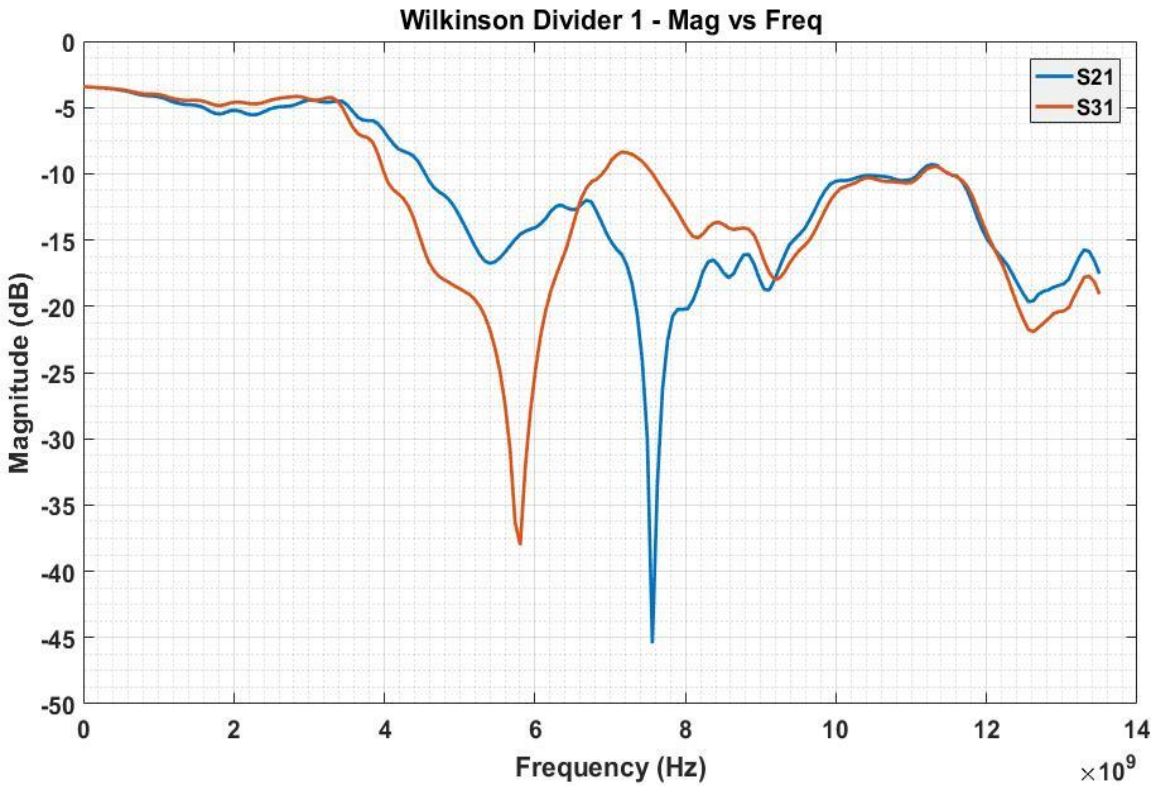

Fig. 45 – Output of the Wilkinson Power Divider used at the input

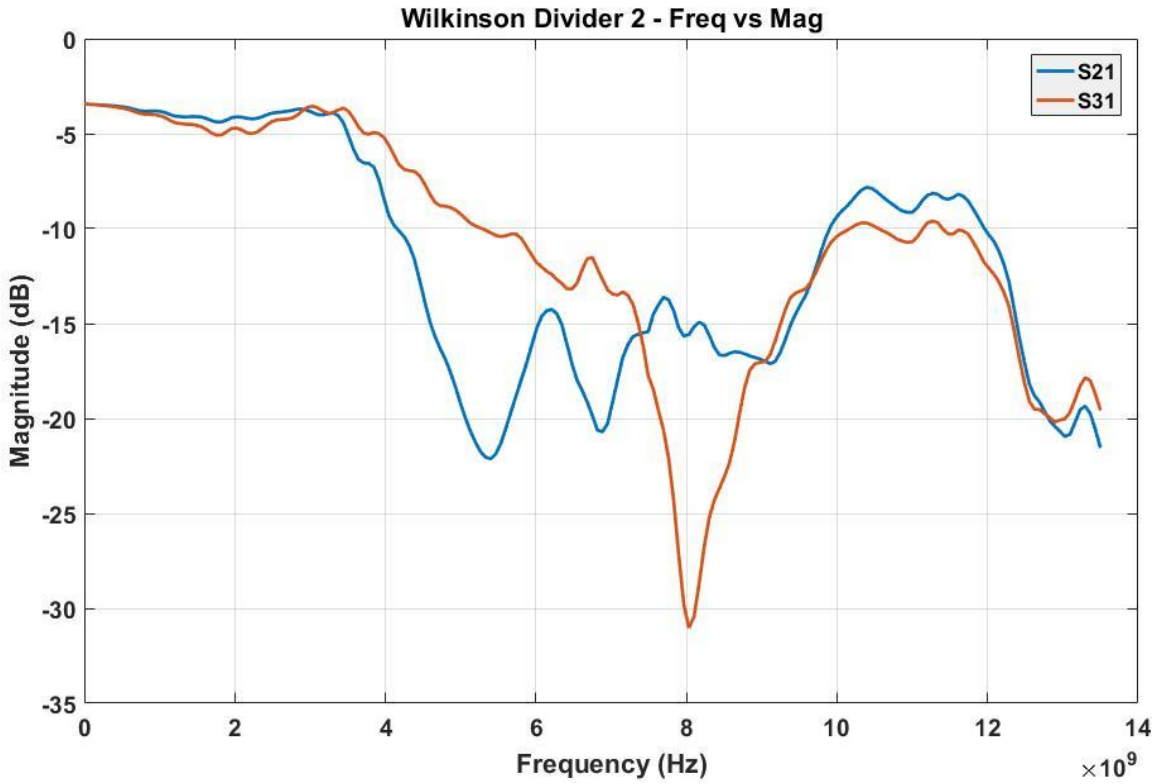

Fig. 47 – Output of the Wilkinson Power Divider used at the output

A resistive power divider/combiner was also designed and fabricated. The lumped elements used in the design were parasitic models provided to the university by Modelithics, Inc. The design was considered because of its large bandwidth. However, the design was not tested as a part of the sensor because of the 6 dB drop that comes as the compromise for the large bandwidth. The simulation model and fabricated board, as well as the performance, of the resistive power divider/combiner is shown in Appendix D.

The reference arm of the sensor was implemented using 2 4-ft long coaxial cables and it included a digital attenuator. A Telemakus TEA13000-12 SN1038 RF attenuator with a range from 0.1 – 13 GHz was used within the reference path of the sensor. The attenuator has an 18 dBm max input and a 30 dB range for attenuation.

The measurement arm included a section of transmission line. Two transmission lines were fabricated and with one as being a meandered line. The meandered line has a longer electrical length which presents the potential for increased sensitivity for humidity measurements. The measurement sections and the measured S_{21} plots are shown in figures 48 and 49.

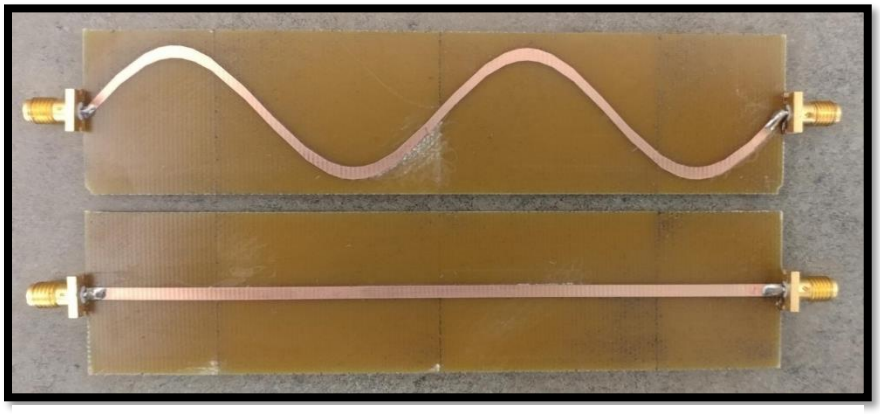

Fig. 48 – Transmission lines used for the measurement section

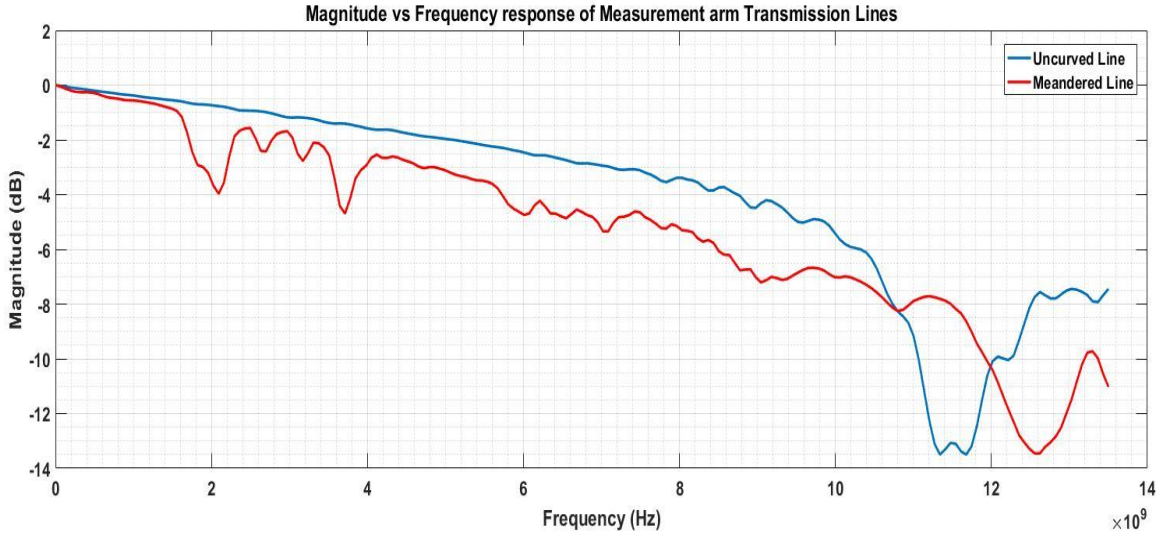

Fig. 49 – Measured S_{21} of the measurement section

CHAPTER SEVEN

Experimental Results of the Ice Cloud Sensor

Ice Cloud Sensor Test Set-up and Results

The ice cloud sensor was tested using the LFACT. To simulate ice clouds, water-based clouds were created with the aid of a spray bar and nozzle system. The flow stream of distilled water covered a range from 0.11 mL/s (25 milli gallons per minute (mGPM)) to 0.61 mL/s (140 mGPM). A Flow Technologies-Linear Link Omniflow model was used to measure the flow stream and was calibrated in milli-gallons per minute. A pitot tube was utilized to determine the pressure in the measurement section of the LFACT. Pitot tubes measure fluid static pressures by calculating the difference between the stagnant and static pressures of the fluid [24]. Humidity measurements were supplied by an Omega-iBTHX humidity sensor. The humidity sensor was mounted about 3 meters from the front of the LFACT.

An Anritsu MS46122A Vector Network Analyzer (VNA) was used for analyzing the scattering parameters of the system and tracking of null frequencies of interest. The VNA is a 2-port device that covers a frequency range from 1 MHz to 20 GHz. The tracking and measuring of null frequencies was automated using the ShockLine program of the VNA and MATLAB.

Fig. 50 – LFACT system at the Baylor Research and Innovation Collaborative (BRIC)

Test runs with the LFACT took an average of 30 minutes. A single test run was taken each day to remove the increased humidity of the room after experiments as a variable. Flow streams were adjusted using valves connected to the spray bar and nozzle system. About 15 seconds was allowed for the stabilization of the flow stream before data was taken. The data acquired was then processed using MATLAB to determine if the sensor was sensitive to changes in the flow rate which determine the cloud density.

Initial experimentations using the Magic Tee coupler and the parallel plate waveguide revealed that the structure was not effective for making ice cloud measurements. Though it possessed the sensitivity required, water droplets accumulating on the inner walls of the measurement arm caused very large frequency shifts that overshadowed the low-volumetric changes of the clouds. A horn antenna placed over the tunnel and a reflector mounted under the tunnel for use as the measurement section was the next design solution tested. This design did not have a direct contact with the

measurement environment, but was unable to detect flow changes in the tunnel. Figure 51 shows a model with the flat plate reflector underneath the Plexiglas.

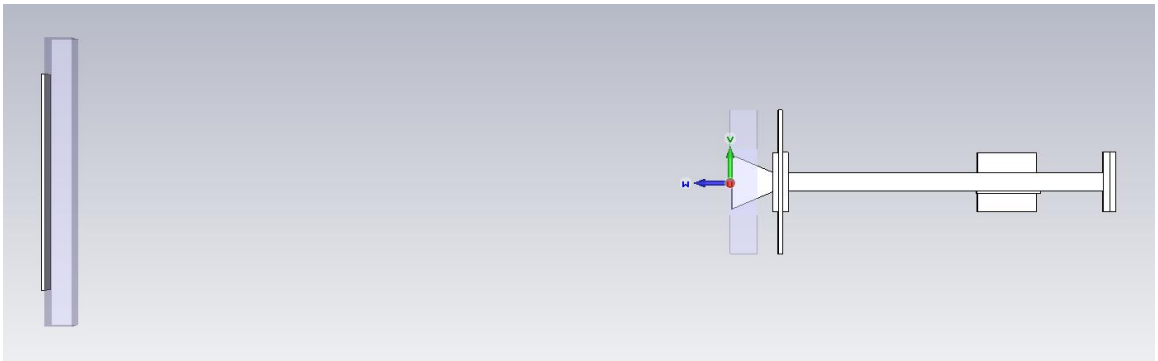

Fig. 51 – Model of the Horn antenna Magic Tee set-up with flat plate reflector (Rotated 90 degrees to the right)

Additional experimentations involved more antennas and other reflector types in hopes of achieving increased sensitivy to the flow changes. A number of tests used two small horn antennas mounted horizontally across the mesurement section of the LFACT and opposite each other. Other tests were performed using a larger horn antenna, HRN-0118, pointed towards corner and parabolic reflectors. The reference arm of the sensor was implemented using 2 4-ft long coaxial cables that included the Telemakus TEA13000-12 SN1038 RF attenuator. Waveguide-to-coax adapters were used in conjunction with the magic tee coupler to include the digital attenuator in the reference path.

The test results of the experiments mentioned above were unfavorable because flow changes were still not perceptible. Changes in water-based cloud density could not be sufficiently tracked by the sensor. The change in electrical length of the sensing path

were not detectable by the sensor because the volume fractions of water droplets in the flow stream was too small.

The results showed the sensor to be more sensitive to the increasing humidity of the room. A change in the test setup is currently being discussed since an enclosed measurement enviroment would not be what the sensor has to encounter. Coupling energy through a 0.7 in thick plexi glass for measurement purposes is a problem that will not be presented to the sensor in a real-world situation. Fig. 52 shows a linear regression of the data with a poor correlation between the predicted and actual flow rates. Fig. 53 shows the results of a time of flight test with undistinguishable changes in phase from varying the flow rate in the tunnel.

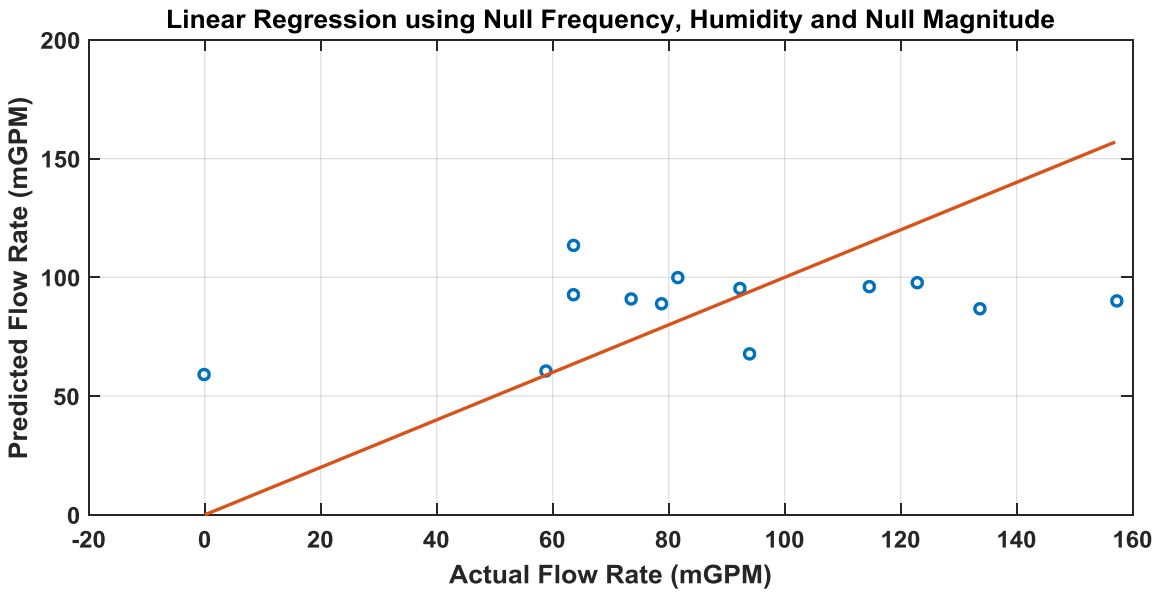

Fig. 52 – Linear Regression of Data using larger Horn Antenna and Corner reflector

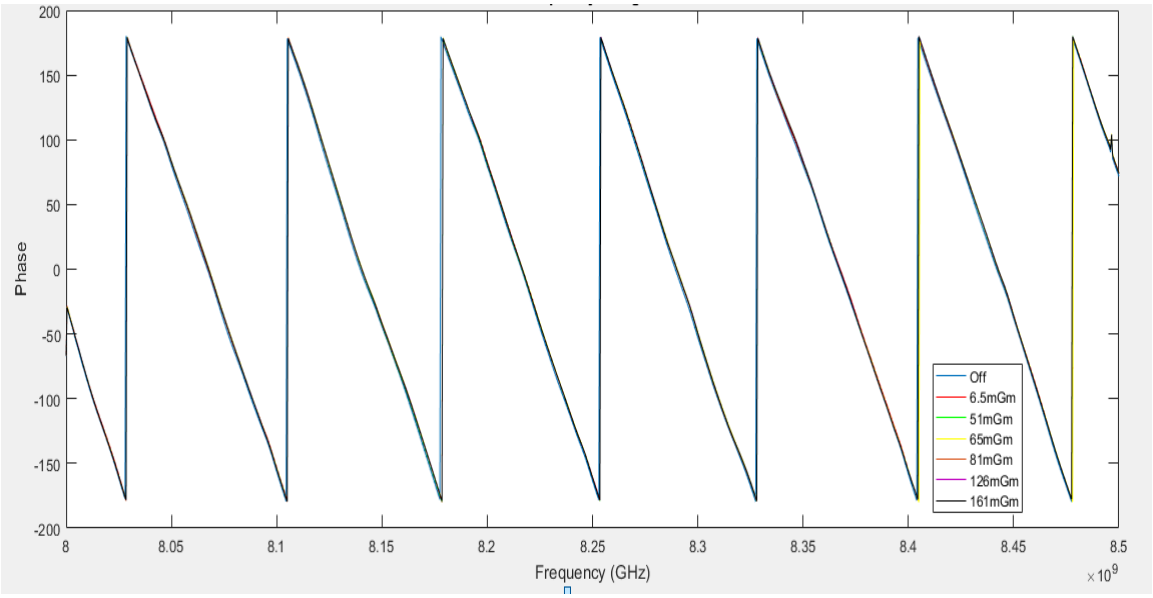

Fig. 53 - Phase Offset plot using two Horn Antennas

Humidity Sensor Test Set and Results

The Anritsu MS46122A VNA created the source signal for the interferometer-type sensor and also tracked changes in the electrical length of the measurement section caused by the change in humidity. Port one of the VNA was connected to the input power divider and port two to the output combiner. Equal lengths of coaxial cables were used to create the measurement and reference paths of the sensor. The uncured or meandered line was included as the measurement section of the measurement path.

For testing the sensor, 500 mL of tap water was heated above 100 °C in a microwave and placed next to the microstrip line measurement section inside the ETC. The steam from the boiling water was used to increase the humidity of the testing environment. An omega OM-90 series temperature and humidity data logger was also placed inside the ETC and tracked the temperature and humidity.

The temperature of the logger is measured to an accuracy of ±0.3 °C over a temperature range of 5 to 60 °C (41 to 140 °F) and ±2.0 °C over for the range of -30 °C to 80 °C (-22 to 176 °F). Relative humidity (RH) is measured to an accuracy of ±3.0 % over the 20 % to 80 % RH range and ±5.0 % RH over the 0 to 100 % RH range.

Test runs lasted for a total of 15 minutes. 5 minutes of data was taken with the VNA and the data logger before a beaker of boiling water was placed into the ETC to increase the humidity. An additional 5 minutes of data was taken with the beaker present before it was removed. The door of the ETC was then left opened to reduce the humidity of the environment for the final 5 minutes of the test. Fig. 54 shows a low frequency test of the sensor.

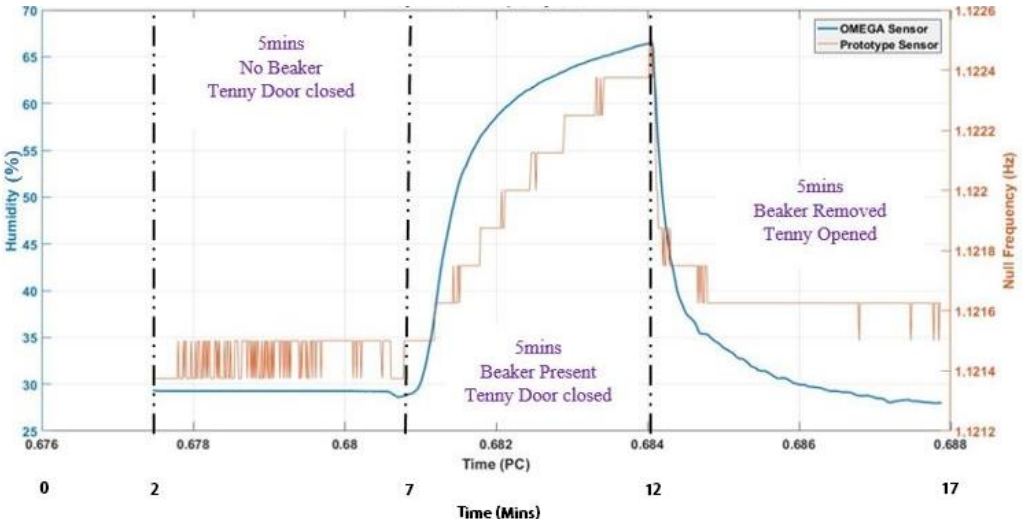

Fig. 54 - Humidity and Null Frequency versus Time (Low Frequency Test)

The first test of the sensor based on a tracked null around 1.22 GHz tracked with the humidity, but lacked the resolution desired. Data points were taken each second and a MATLAB interpolation of the logger data and computer time was used to obtain the humidity values of the prototype sensor. It is noteworthy to mention that the resolution of

the VNA was not set very high (500 points over a 50 MHz span) to reduce data acquisition time from frequency sweeps.

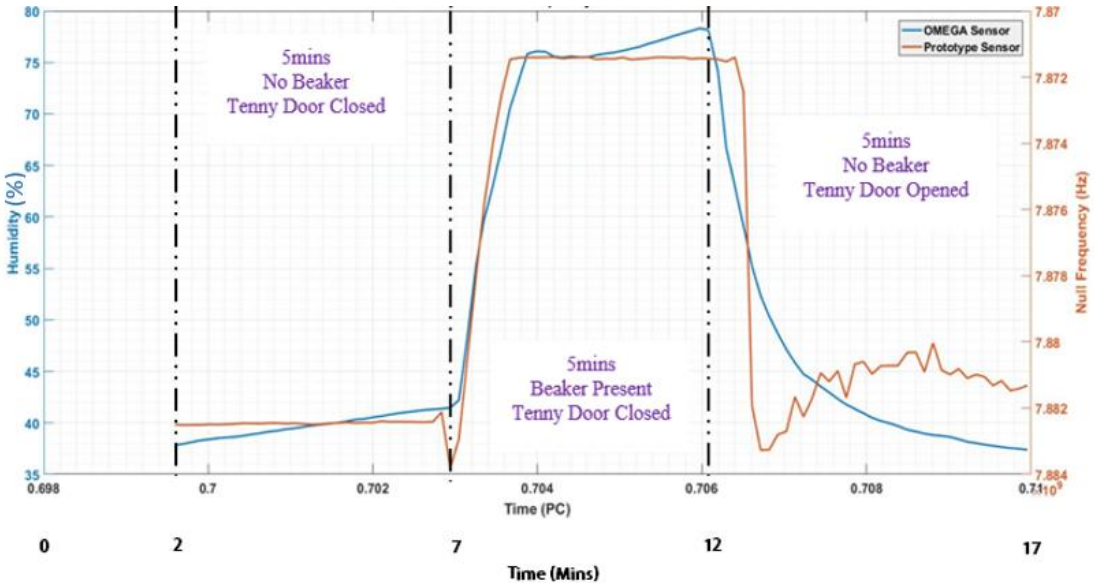

Fig. 55 - Humidity and Null Frequency versus Time (High Frequency Test)

Fig. 55 shows a higher frequency test of the humidity sensor based on a tracked null around 7.88GHz. A single data point was taken every 10 seconds for the duration of the test. The resolution of the VNA was set much higher (5000 points over a 25MHz span) for the second test. The resolution of the sensor was higher compared to the previous test, but the sensitivity of the OMEGA sensor to humidity changes of the chamber was better.

CHAPTER EIGHT

Conclusion

A hybrid planar antenna for use in a microwave radiometer system that detects the accretion of ice particles in turbofan jet engines has been developed and demonstrated. Processed data from the sensor showed that the use of the hybrid antenna produced improved sensitivity and about twice the resolution compared to that of the rectangular patch antenna. The hybrid antenna had a voltage magnitude difference that was 0.1V greater than that of the rectangular patch.

Placing ice and water in the near-field of the radiometer antenna changes its impedance and the noise temperature of the system which is shown in the radiometer's output. The results of the system presented are a function of the antenna's varying impedance as well as the emissivity. Future work will be required to quantify the percent impact due to the antenna's impedance versus the emissivity of ice and water.

Future experimentations including changing the polarization of the antenna, testing in "quieter" channels and using a process seal insert for the antenna are also being considered. The sensor was tested at 10GHz since previous tests with the radiometer revealed that a center frequency of 10 GHz exhibited the largest voltage range which corresponded to the highest sensitivity to temperature change. However, additional experimentations need to be moved to 10.6 GHz which is a part of the spectrum allocated for Radio Astronomy and other passive space research projects.

While the science and sensing technique supports our ability to detect ice crystals with the cloud sensor, problems with the increasing humidity of the room need to be

addressed. The increasing humidity masks the slight changes in flow rate that the sensor has to detect. An additional, precise humidity sensor could be used to compensate for the increasing humidity of the room. The measurement set-up also needs to be improved. The measurement path signal has to penetrate two plates of plexi-glass which reduces the sensitivity of the system. The plexi-glass ($\varepsilon_r \approx 3.4$) of the measurement section of the LFACT causes a substantial amount of reflection for the microwave sensor. A solution would be a measurement section constructed of a material with a permittivity closer to free space. A rigid, water-resistant Styrofoam ($\varepsilon_r \approx 1.11$) could be tested.

The interferometer sensor showed a strong sensitivity to the humidity of the lab. An adjusted R^2 value of 0.796, with a standard error of 0.752%, was shown for the calibrated response of the sensor for relative humidity at room temperature and pressure. This discovery speaks to the sensitivity and capability of our sensing technique since humidity changes require more sensitivity for detection than ice particles.

APPENDICES

APPENDIX A

Antenna Farfield Directivity

The azimuth and elevation plots, respectively, of the directivity simulation at 9.7 GHz is shown below. The simulations were performed using CST microwave studio.

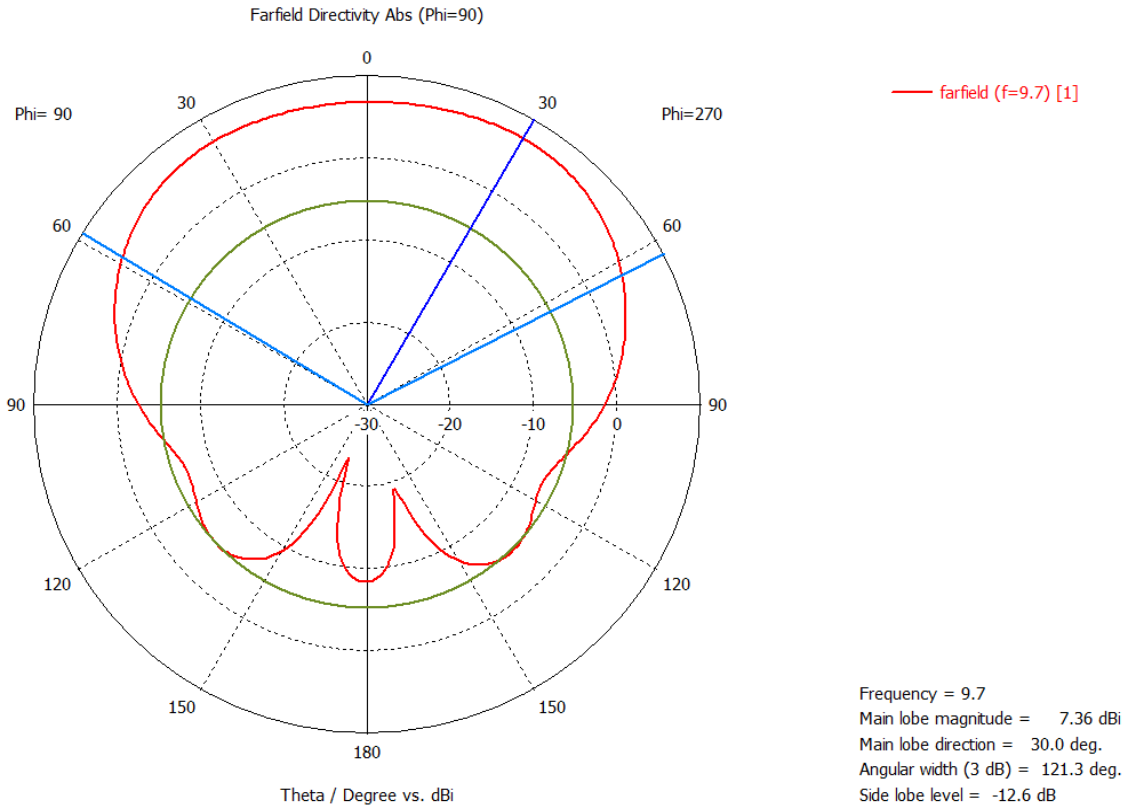

Fig. A.1 - Azimuth Plot

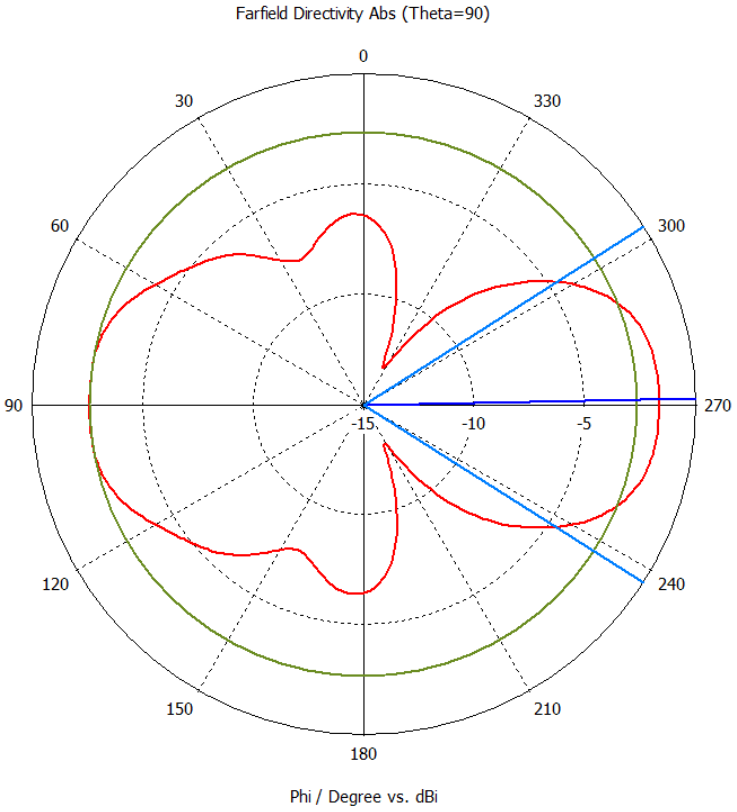

farfield (f=9.7) [1]

Frequency = 9.7
Main lobe magnitude = -1.66 dBi
Main lobe direction = 271.0 deg.
Angular width (3 dB) = 65.0 deg.
Side lobe level = -1.0 dB

APPENDIX B

Other Planar Antenna Designs Considered

The figures below show a number of other designs simulated and their results before the hybrid antenna was developed. The simulations were performed using CST microwave studio.

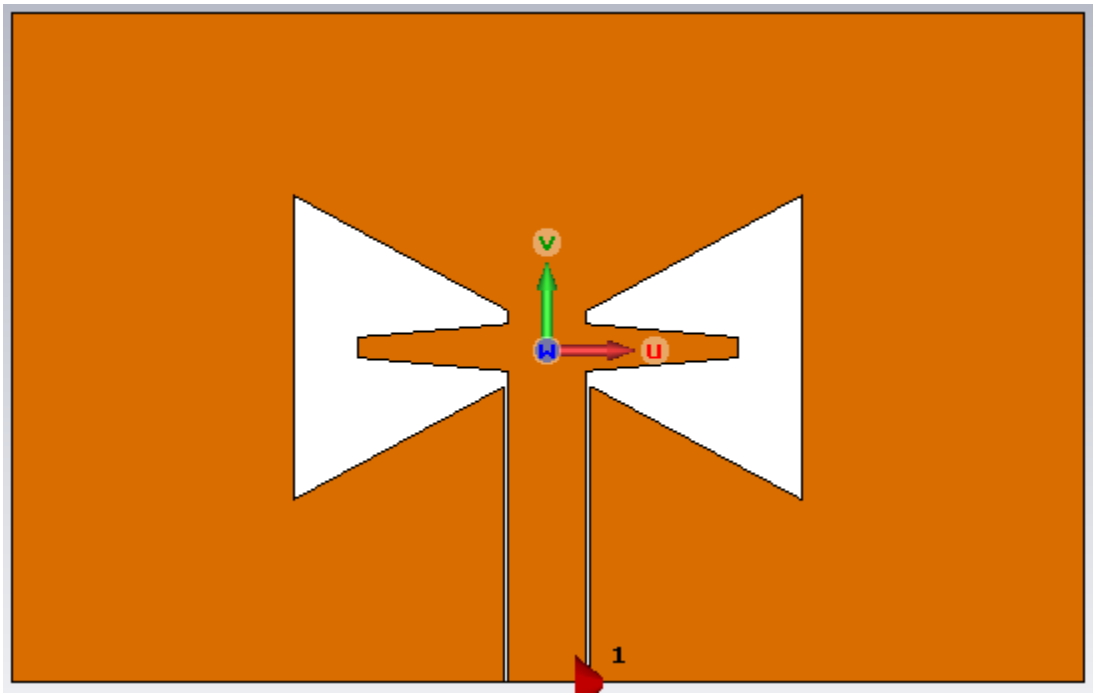

Fig. B.1 – Bowtie Antenna Model

The antenna model in Fig. B.1 was simulated using a discrete port and did not include a ground plane on the back. Also, the design leaves no room for electrically isolating the antenna from the vanes. The frequency response plot is shown in Fig. B.2.

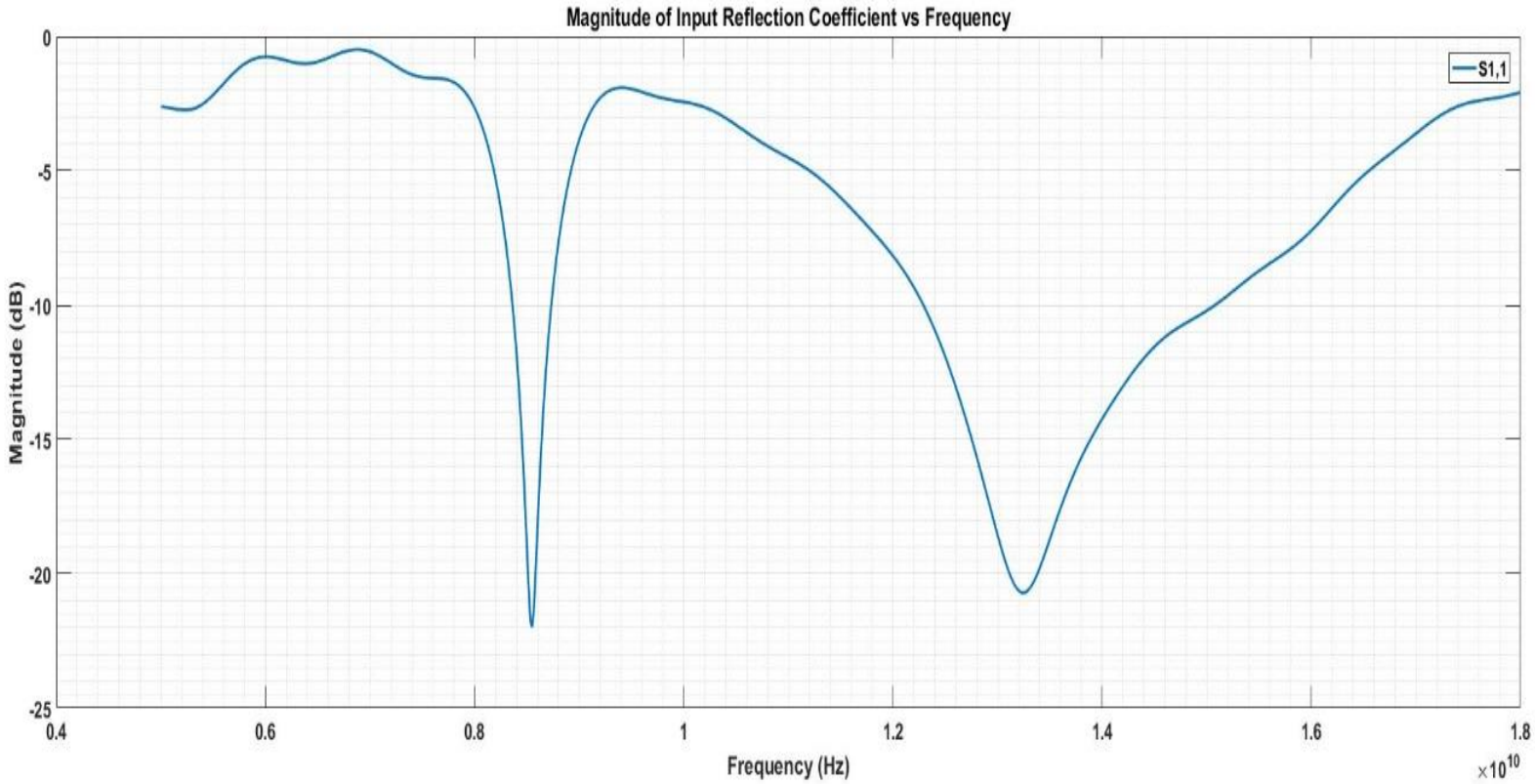

Fig. B.2 – Input Reflection Coefficient Plot

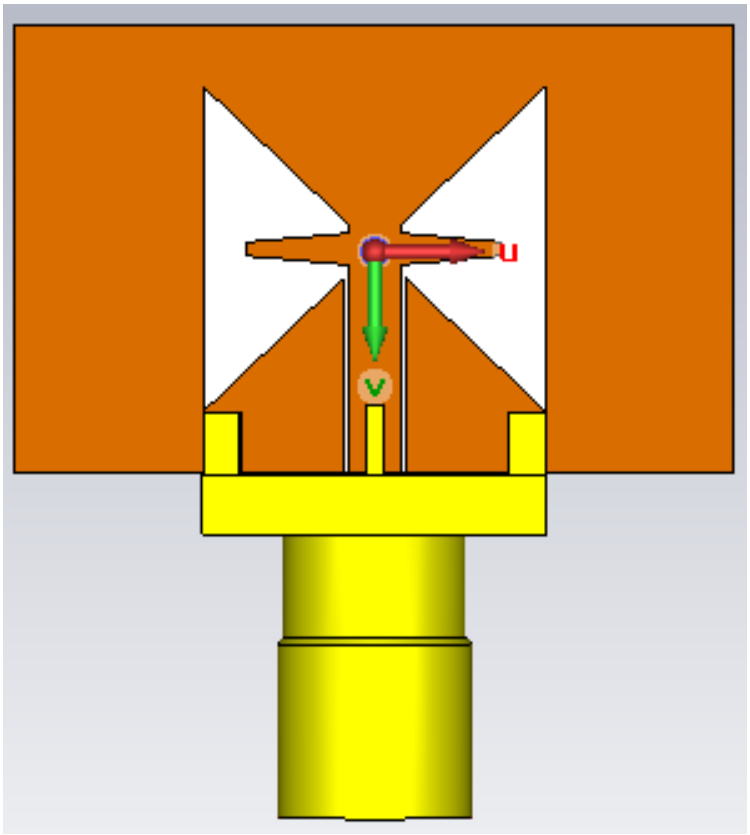

Fig. B.3 – Bowtie Antenna Model

The structure in Fig. B.3 was simulated using an SMA connector and it included a ground plane on the back. The design still left no room for electrically isolating the antenna from the stator vanes. The frequency response plot is shown below in Fig. B.4.

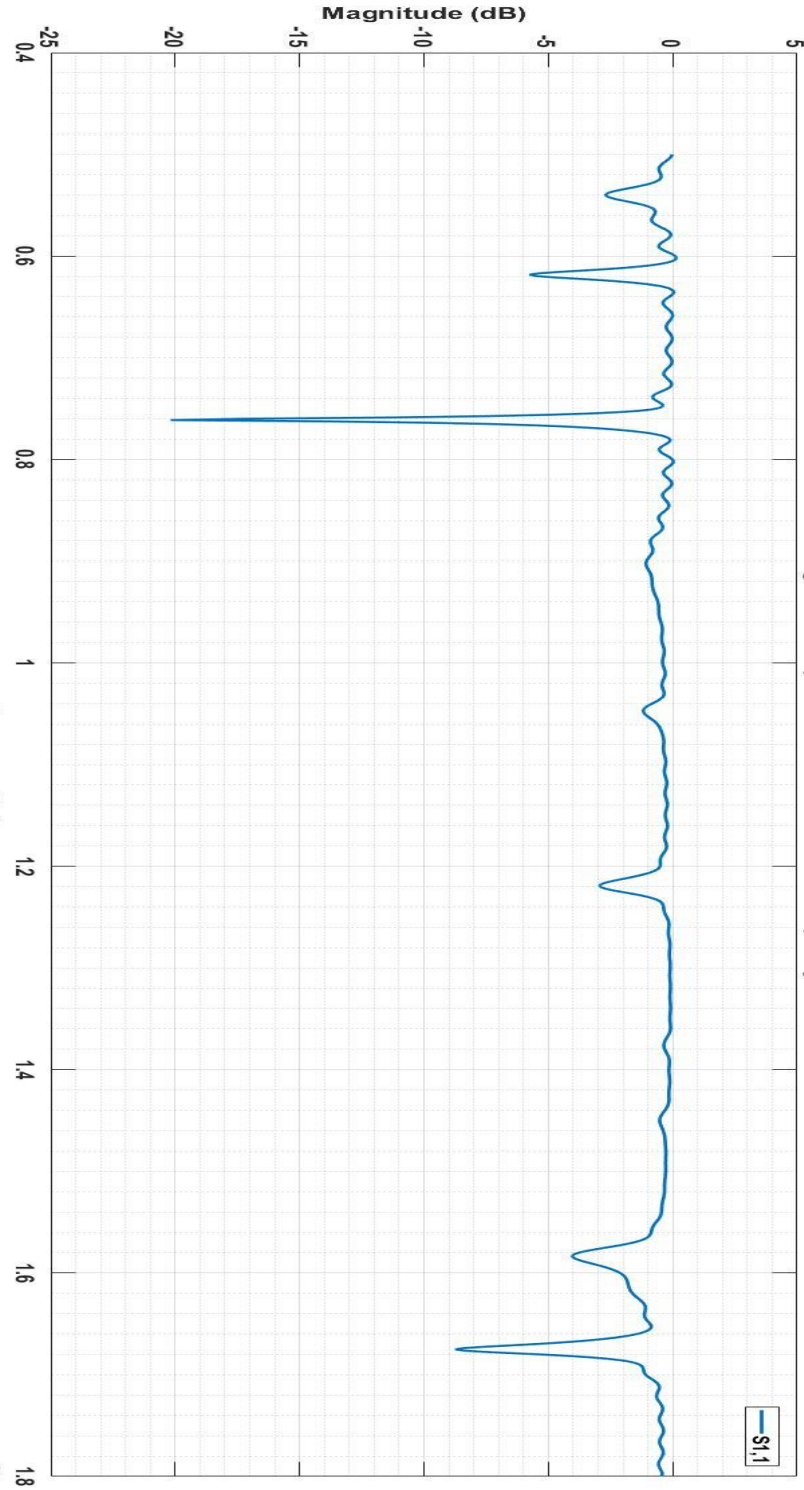

Fig. B.4 - Input Reflection Coefficient Plot

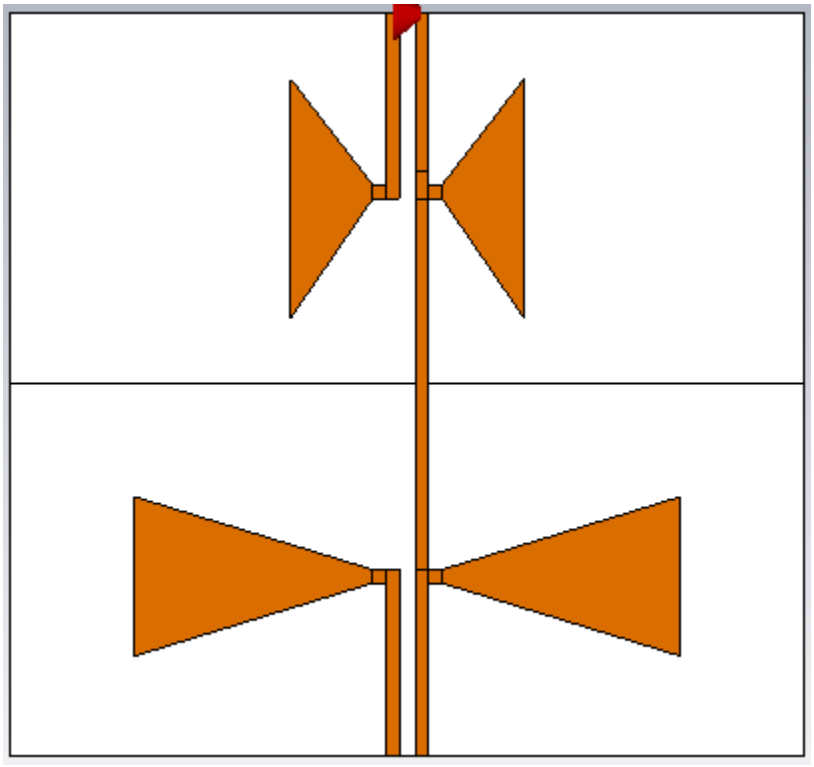

Fig. B.5 – Bowtie Antenna Model

The bow-tie antenna model in Fig.5 was simulated using a discrete port and it did not include a ground plane on the back. Also, the huge size of the larger bow-tie made it an unusable option since it was larger than our design aperture size. The frequency response plot is shown below in Fig. B.6.

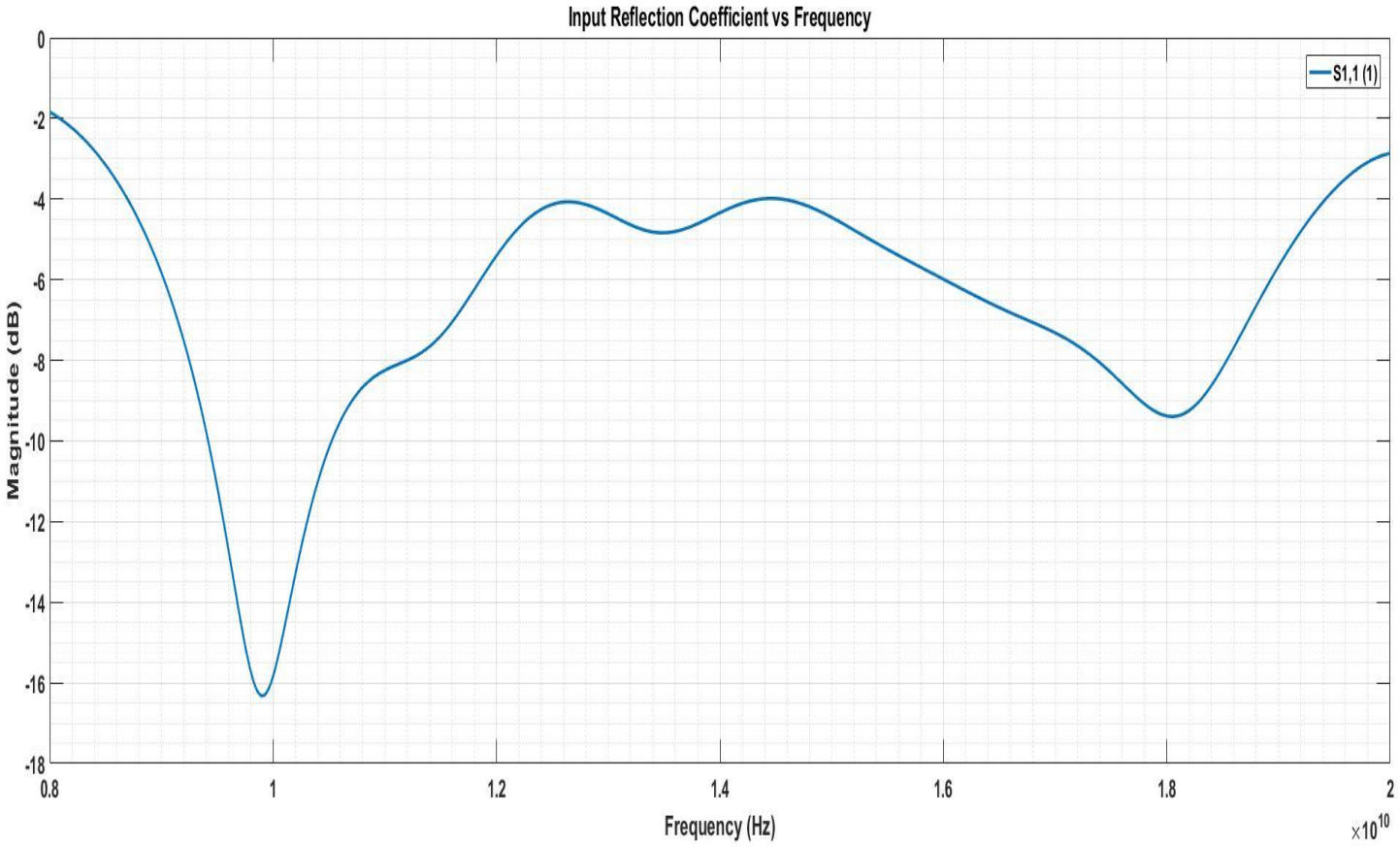

Fig. B.6 - Input Reflection Coefficient Plot

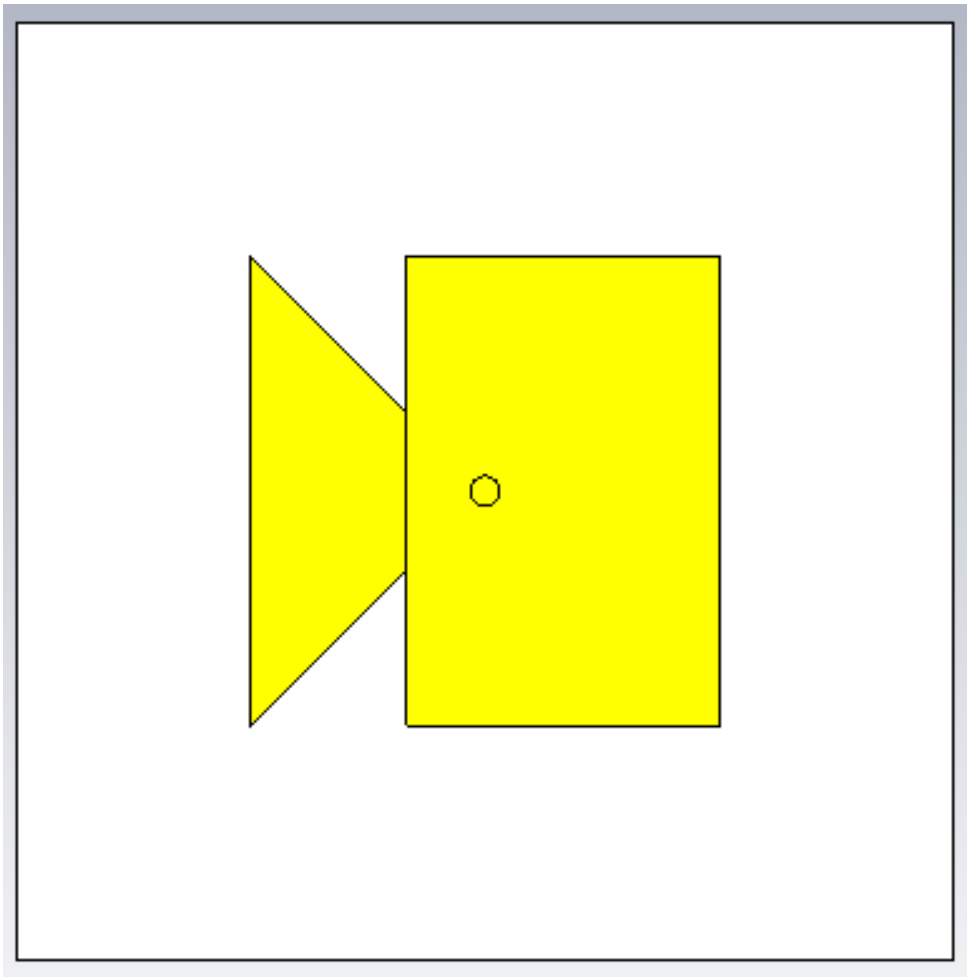

Fig. B.7 – Hybrid Planar Antenna Model

The structure in Fig. B.7 was the first to be simulated in a series of designs that lead to the hybrid planar antenna. It was simulated using a digital SMA connector. The frequency response plot is shown in Fig. B.8.

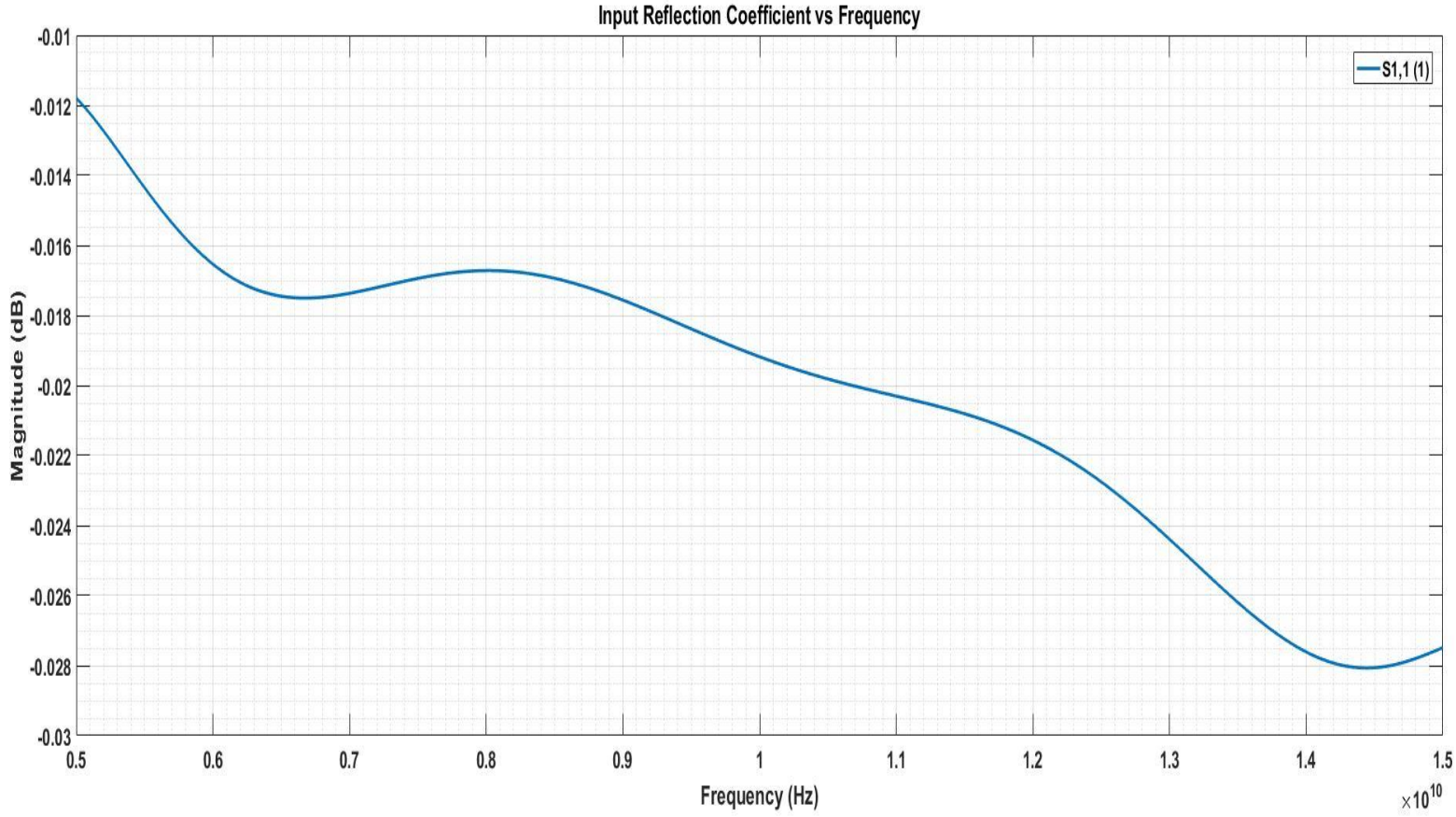

Fig. B.8 - Input Reflection Coefficient Plot

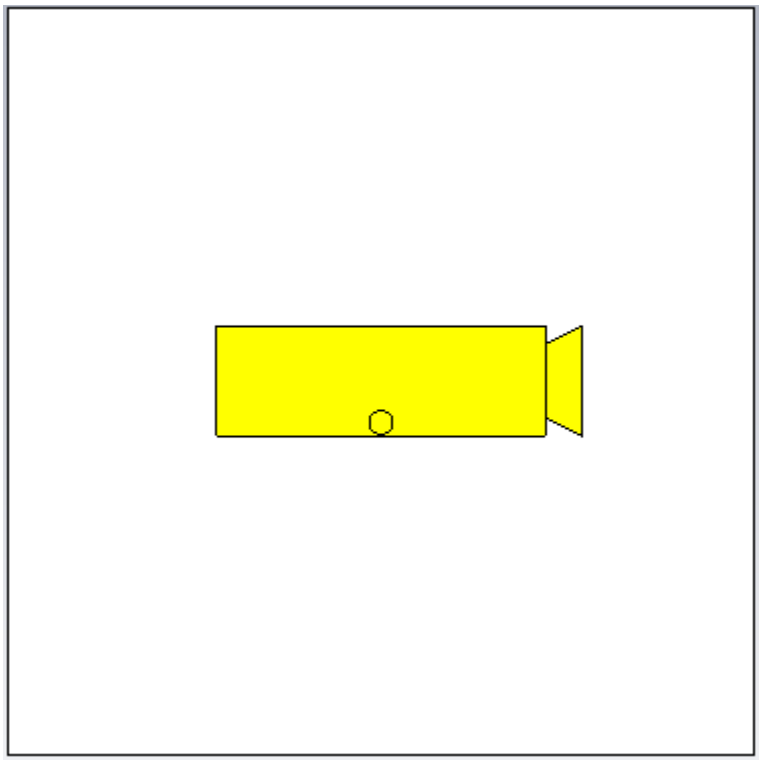

Fig. B.9 – Hybrid Planar Antenna

The antenna model in Fig. B.9 was in the final group of structures simulated before the current hybrid planar antenna was designed. It was simulated with a digital SMA connector and included a ground plane on the back. The frequency response plot is shown in Fig. B.10.

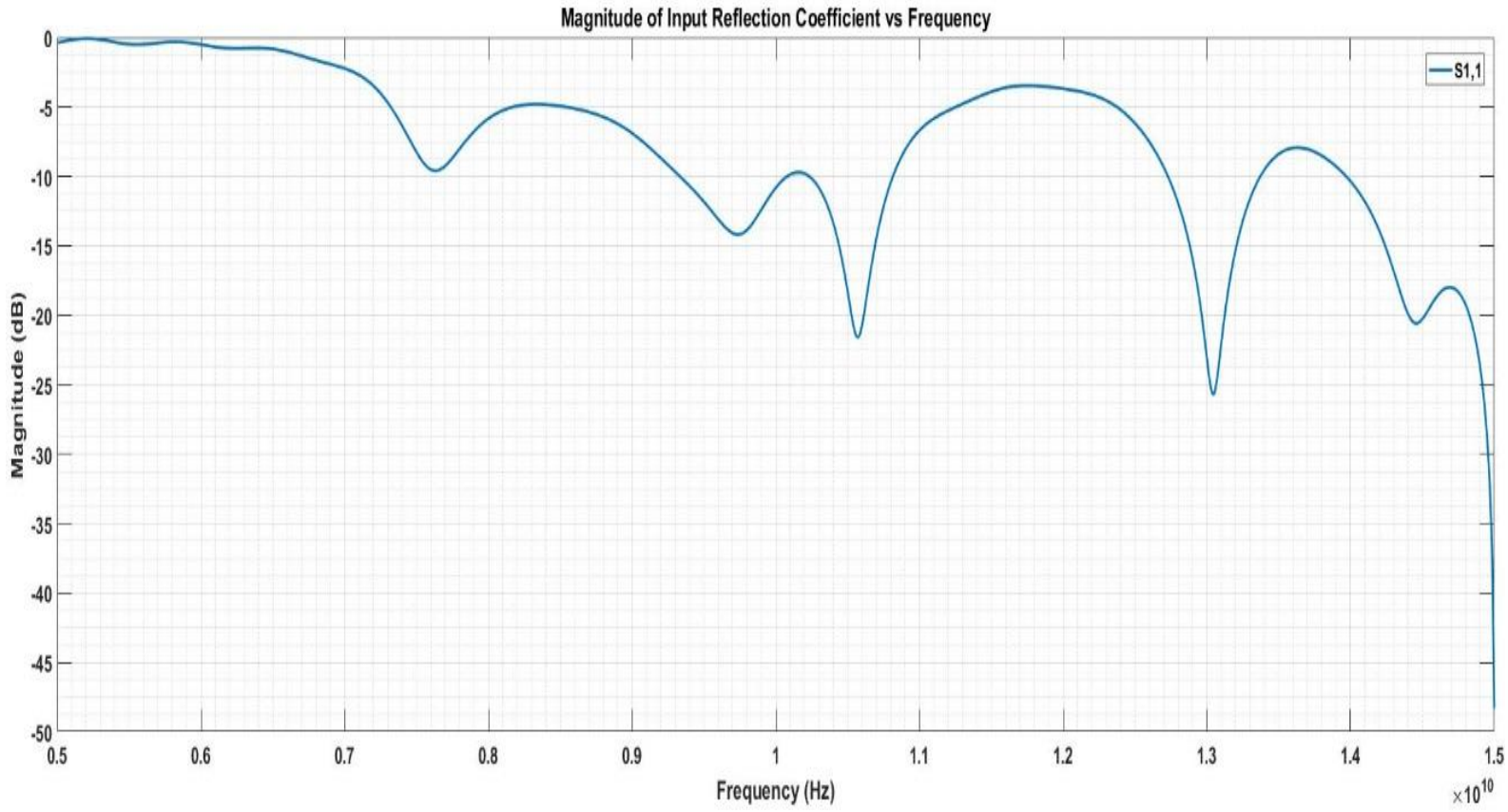

Fig. B.10 - Input Reflection Coefficient Plot

APPENDIX C

Parametric Sweeps of the Hybrid Planar Antenna

The figures below show the results of the parametric sweeps taken in the characterization and study of the antenna. The sweeps were performed using CST microwave studio.

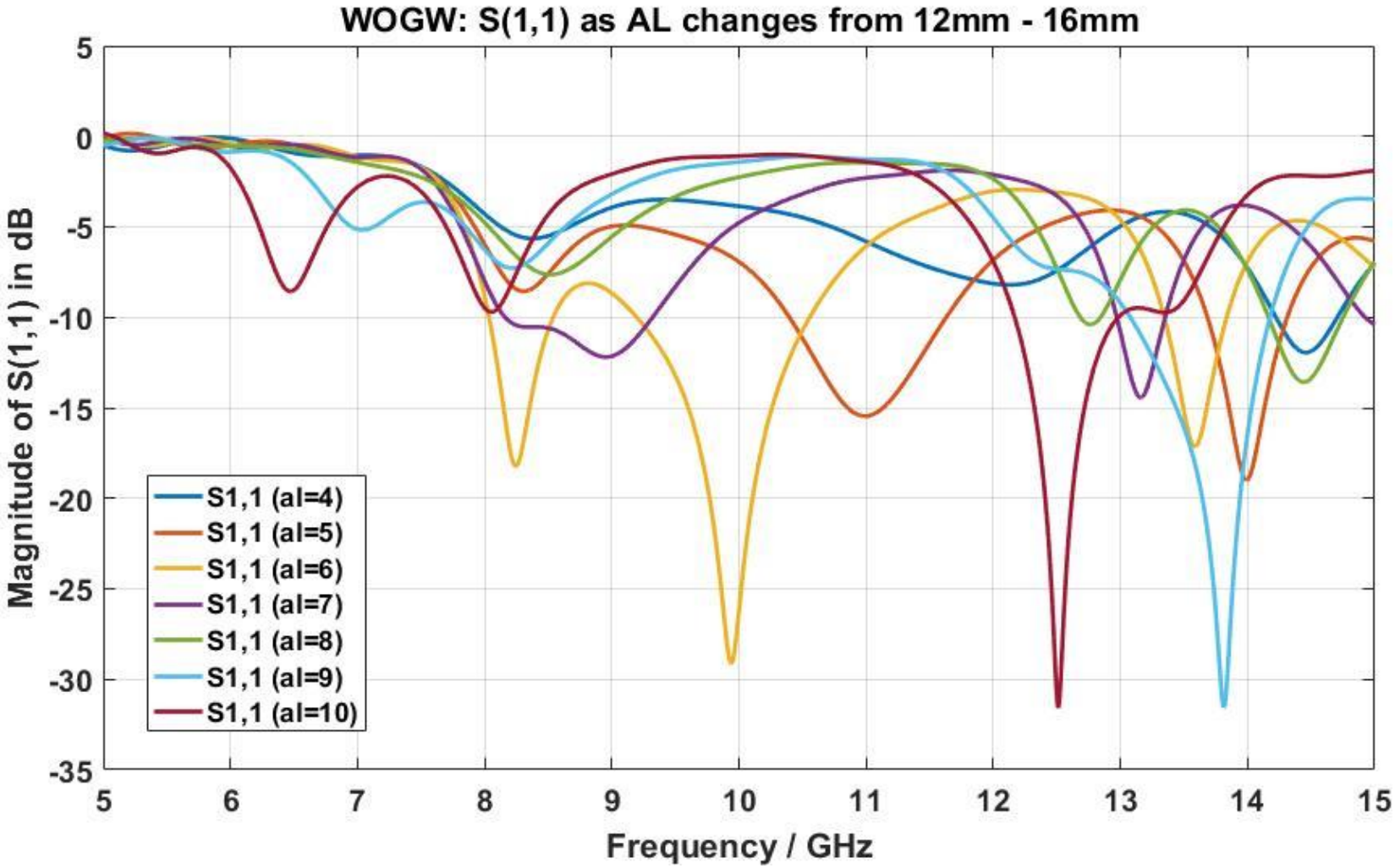

Fig. C.1 - Varying Antenna Length

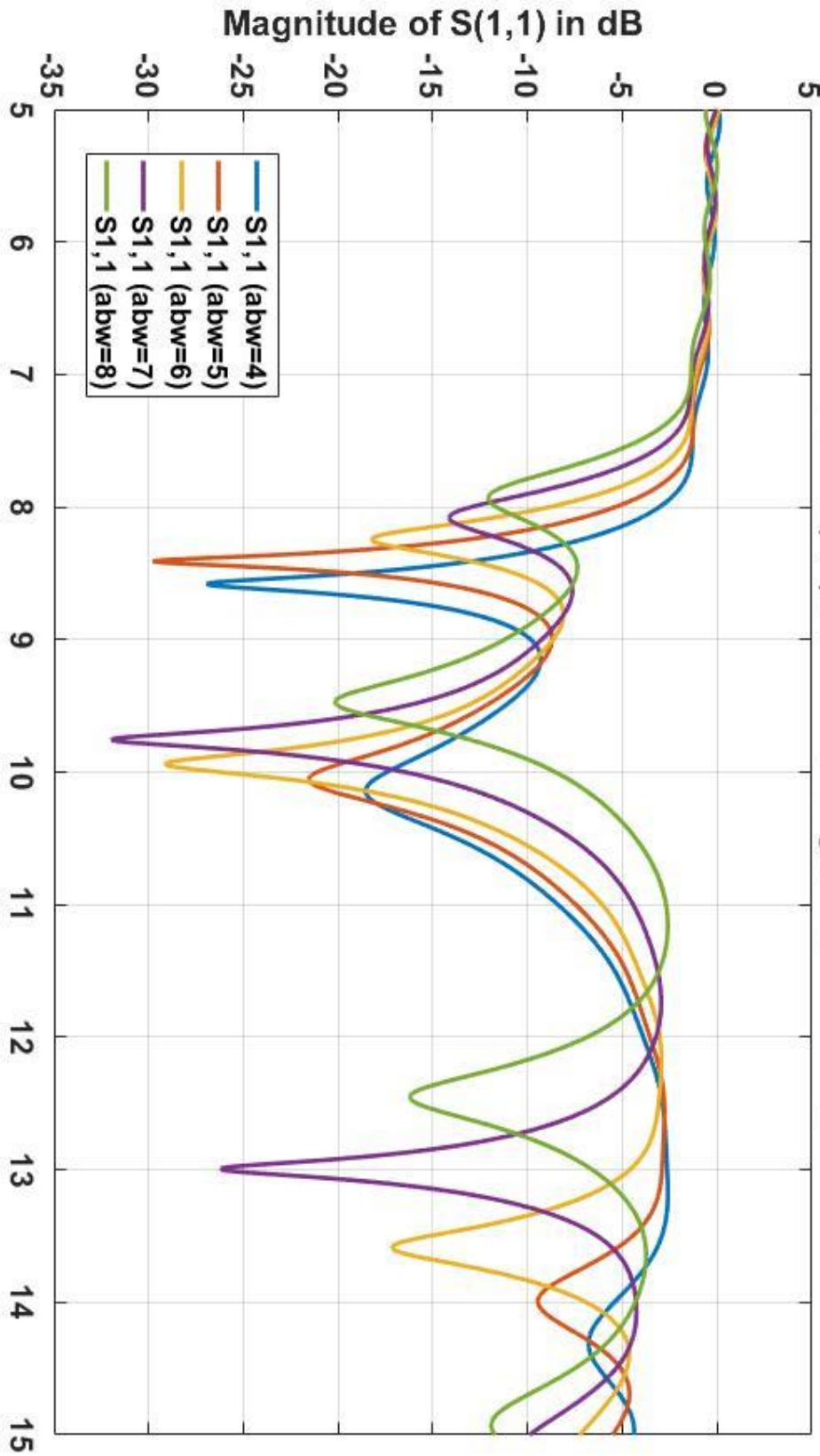

Fig. C.2 - Varying Antenna Bow Width

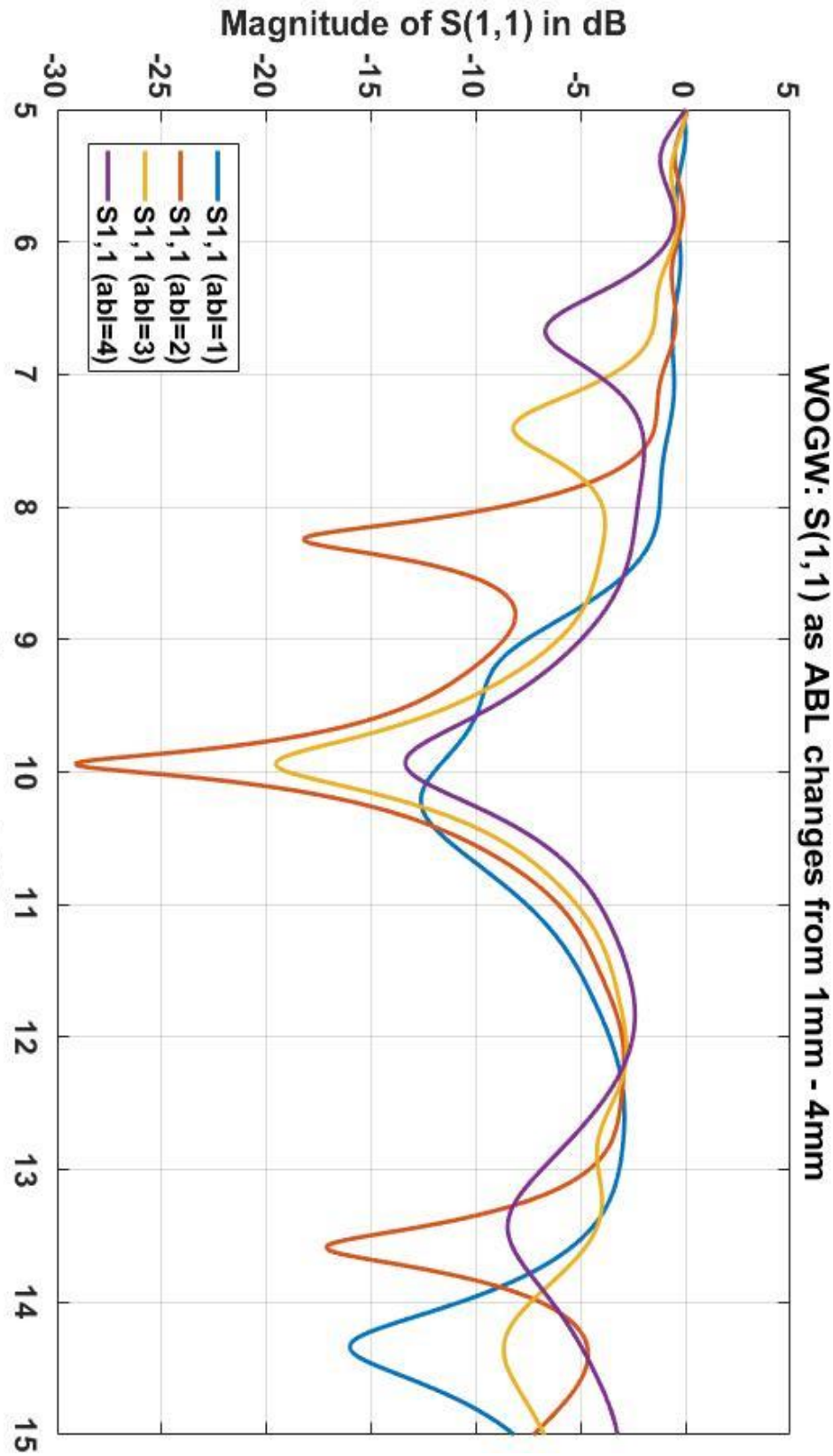

Fig. C.3 - Varying Antenna Bow Length

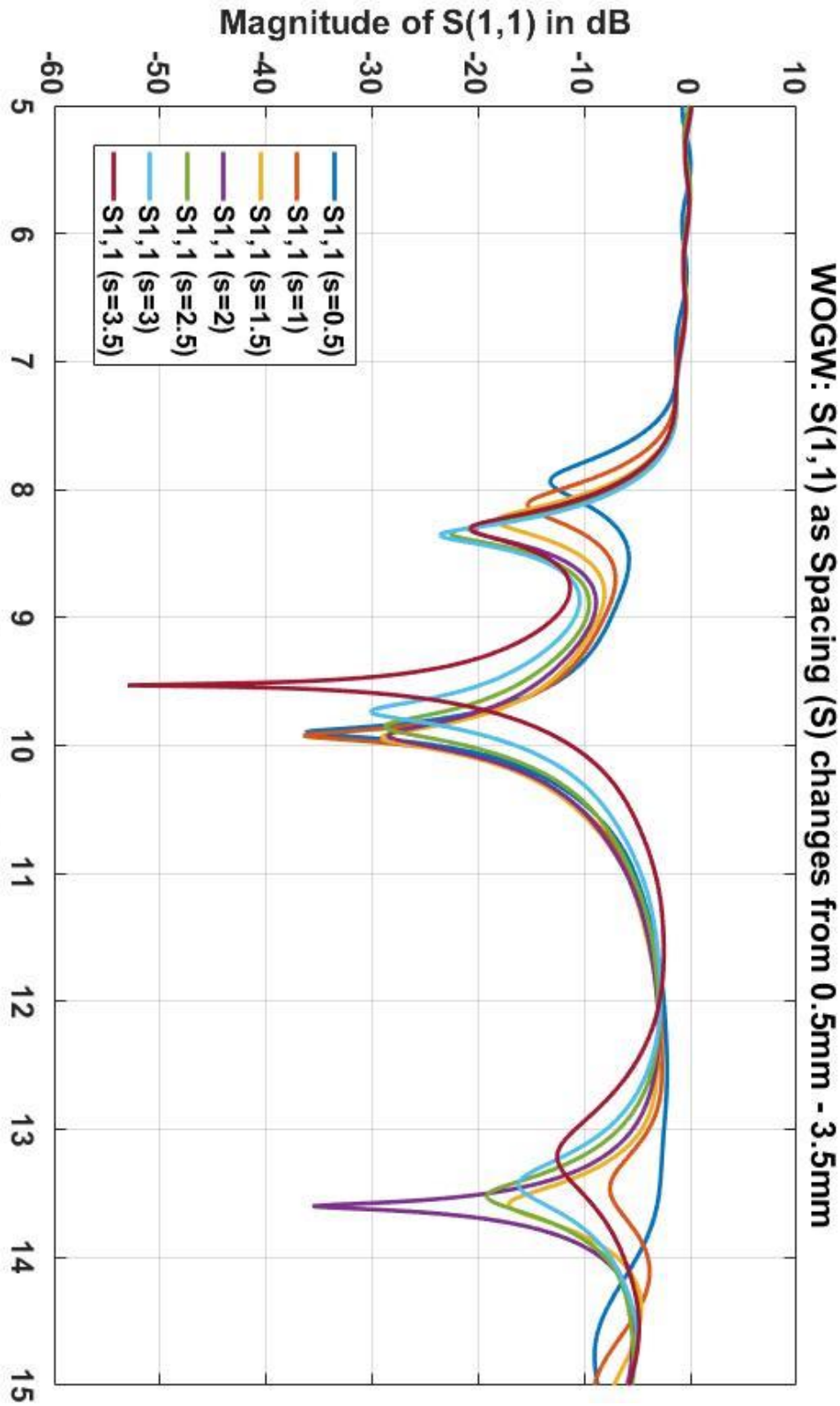

Fig. C.4 - Varying Antenna Bow Spacing

APPENDIX D

Design Model of the Resistive Power Splitters/Dividers

The schematic below shows the parasitic lumped elements model of the Resistive Power Dividers tested for the humidity sensors. The schematic was designed in ADS (Advanced Design System).

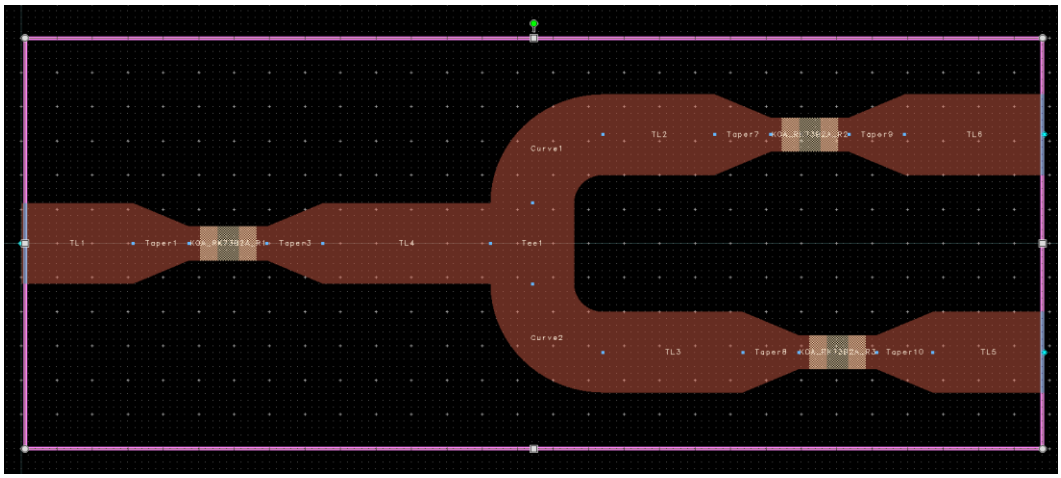

Fig. D.1 - Layout of the power

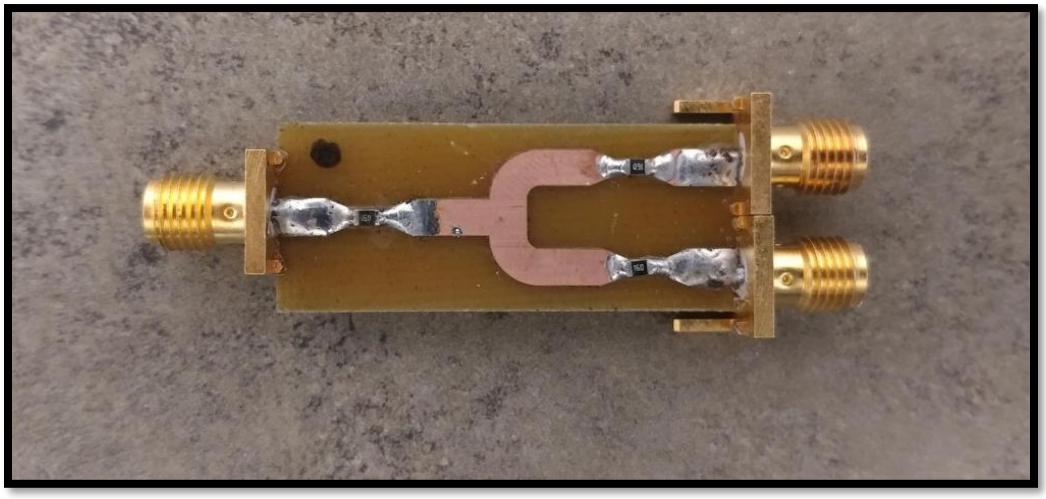

Fig. D.2 - Fabricated power Splitter

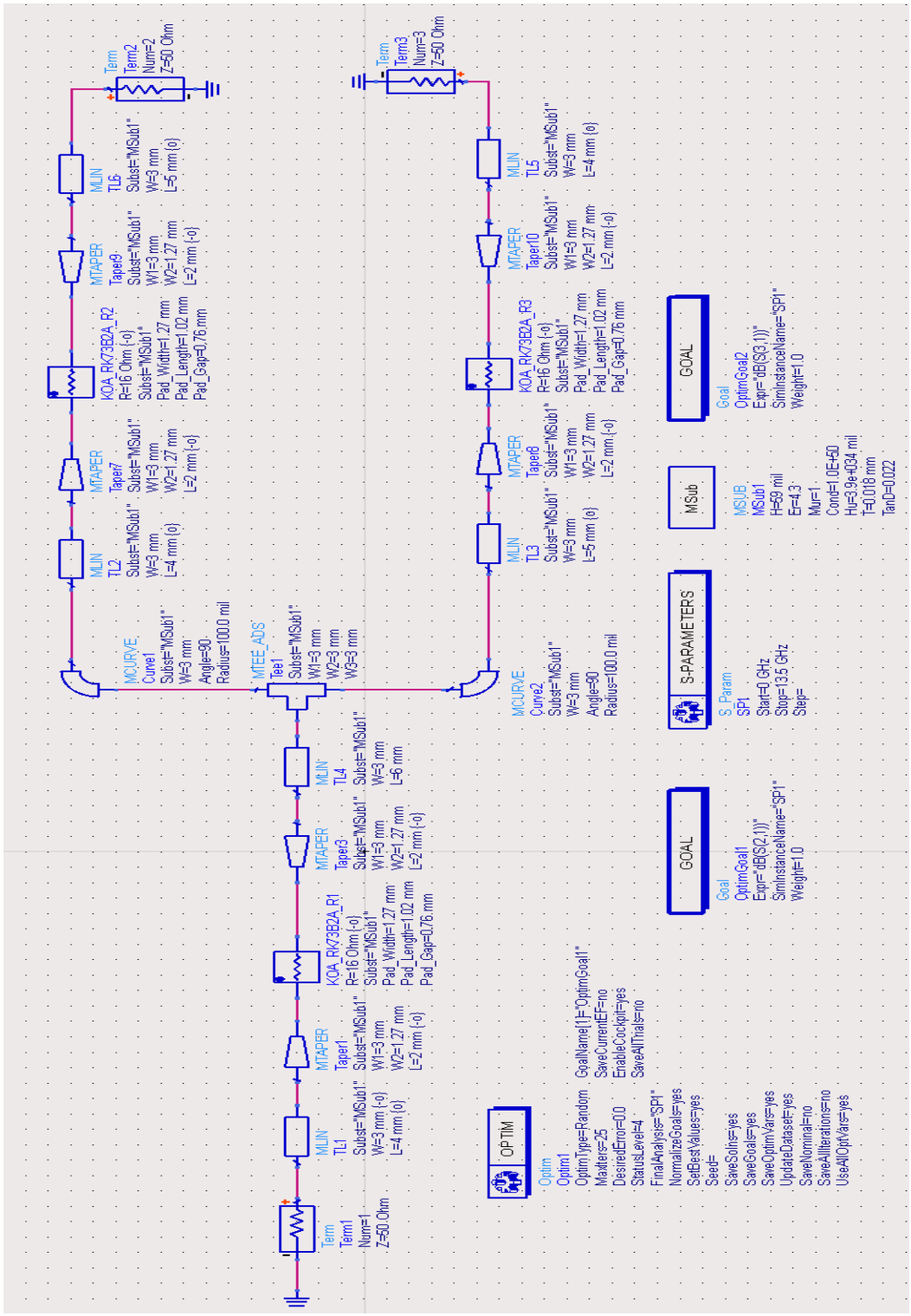

Fig. D.3 - Schematic of the power Splitter

BIBLIOGRAPHY

[1] J. G. Mason, J. W. Strapp and P. Chow, "The Ice Particle Threat to Engines in Flight," in 44th AIAA Aerospace Sciences Meeting and Exhibit, Reno, 2006

[2] T. Trapp, “Measuring Ice Accretion with a Microwave Radiometer,” Research Master thesis, School of Engineering and Computer Science, Baylor Univ., Waco, TX, 2017.

[3] P. Anatoly, Radiometry in modern scientific experiments. New York, NY: SpringerWien, 2011. p. 1.

[4] N. Skou and D. L. Vine, Microwave Radiometer Systems, Norwood, MA: Artech House, Inc., 2006.

[5] Stewart, Sean M., and R. Barry Johnson. Blackbody Radiation: A History of Thermal Radiation Computational Aids and Numerical Methods, CRC Press, 2016. ProQuest Ebook Central, https://ebookcentral.proquest.com/lib/bayloru/detail.action?docID=4694269. p. 3.

[6] Zhang, Yanguo Li, Qinghai Zhou, Hui. (2016). Theory and Calculation of Heat Transfer in Furnaces - 1.2.1 Description of Radiant Energy. Elsevier.

[7] Saunders, Peter. (2007). Radiation Thermometry - Fundamentals and Applications in the Petrochemical Industry - 2.3.1 Planck's Law. SPIE. p. 10.

[8] F. T. Ulaby, R. K. Moore and A. K. Fung, Microwave Remote Sensing: Fundamentals and Radiometry, vol. I, Reading, Massachusetts: Addison-Wesley Pub. Co., 1981, p. 456.

[9] S. J. Goldstein, "A Comparison of Two Radiometer Circuits," in Proceedings of the IRE, vol. 43, no. 11, pp. 1663-1666, Nov. 1955. URL: http://ieeexplore.ieee.org/stamp/stamp.jsp?tp=&arnumber=4055310&isnumber=4055293

[10] Adamy, Dave. (2014). Practical Communication Theory (2nd Edition) - 6.1 Sensitivity. Institution of Engineering and Technology. pp. 93

[11] C. A. Balanis, Advanced Engineering Electromagnetics, Hoboken, NJ: John Wiley & Sons, Inc., 2012, pp. 42, 56.

[12] B. R. Jean, S. McClain, T. Trapp, B. Herrera, T. Shannon and G. Toby, "A microwave interferometer sensor for ice cloud detection and measurement," 2017 IEEE International Workshop on Metrology for AeroSpace (MetroAeroSpace), Padua, 2017, p. 93-96.

[13] M. Niang, M. Bernier, M. Stacheder, A. Brandelik, and E. V. Bochove, “Influence of Snow Temperature Interpolation Algorithm and Dielectric Mixing-Model Coefficient on Density and Liquid Water Content Determination in a Cold Seasonal Snow Pack,” Subsurface Sensing Technologies and Applications, vol. 7, no. 1, p. 5, Apr. 2006.

[14] Antenna Engineering Handbook, 4th ed., McGraw-Hill, New York, NY, 2007, p. 1-9, 7-2,3, 34-14,15.

[15] W. H. Hayt, Jr and J. Buck, Engineering Electromagnetics, 8th Ed. New York, NY: McGraw-Hill, 2010.

[16] L. R. Ballew, *A Microwave Radiometer System for Use in Biomedical Applications,* Waco: Baylor University, 2006.

[17] P. Willems, "LIGO: The laser interferometer gravitational-wave observatory," 2006 Conference on Lasers and Electro-Optics and 2006 Quantum Electronics and Laser Science Conference, Long Beach, CA, 2006, p. 1-2.

[18] P. Hariharan, Basics of interferometry. Amsterdam: Elsevier Academic Press, 2007. p. 4.

[19] C. Haslett, Essentials of Radio Wave Propagation. Cambridge: Cambridge University Press, 2008. p. 86 – 88.

[20] D. M. Pozar, Microwave Engineering, 3rd ed., Hoboken, NJ: John Wiley & Sons, Inc., 2005, p. 28.

[21] B. R. Jean, “A microwave frequency sensor for steam quality,” IEEE Trans. Inst. Meas., vol. 57, no. 4, 2008, p. 751-754.

[22] S. Ramo, J. Whinnery and T. Van Duzer, Fields and Waves in Communication Electronics, Hoboken, NJ: John Wiley & Sons, Inc., 1993. p.560.

[23] Joseph F. White, "Directional Couplers," in High Frequency Techniques: An Introduction to RF and Microwave Engineering, 1, Wiley-IEEE Press, 2004, p.330-331.

[24] AIChE. AIChE Equipment Testing Procedure - Trayed and Packed Columns: A Guide to Performance Evaluation, Wiley, 2014. ProQuest Ebook Central, https://ebookcentral.proquest.com/lib/bayloru/detail.action?docID=1629182.